

Investigation on Young radio AGNs based on SDSS spectroscopy

Mai Liao,^{1,2★} Minfeng Gu,^{1†}

¹*Shanghai Astronomical Observatory, Chinese Academy of Sciences, 80 Nandan Road, Shanghai 200030, China*

²*University of Chinese Academy of Sciences, 19A Yuquanlu, Beijing 100049, China*

Accepted XXX. Received YYY; in original form ZZZ

ABSTRACT

The Gigahertz Peaked Spectrum (GPS) sources, Compact Steep Spectrum (CSS) radio sources, and High Frequency Peakers (HFP) radio sources are thought to be young radio AGNs, at the early stage of AGN evolution. We investigated the optical properties of the largest sample of 126 young radio AGNs based on the spectra in SDSS DR12. We find the black hole masses M_{BH} range from $10^{7.32}$ to $10^{9.84} M_{\odot}$, and the Eddington ratios R_{edd} vary from $10^{-4.93}$ to $10^{0.37}$, suggesting that young radio AGNs have various accretion activities and not all are accreting at high accretion rate. Our young radio sources generally follow the evolutionary trend towards large-scale radio galaxies with increasing linear size and decreasing accretion rate in the radio power - linear size diagram. The radio properties of low luminosity young radio AGNs with low R_{edd} are discussed. The line width of [O III] $\lambda 5007$ core ($\sigma_{[\text{OIII}]}$) is found to be a good surrogate of stellar velocity dispersion σ_* . The radio luminosity $L_{5\text{GHz}}$ correlates strongly with [O III] core luminosity $L_{[\text{OIII}]}$, suggesting that radio activity and accretion are closely related in young radio sources. We find one object that can be defined as narrow-line Seyfert 1 galaxies (NLS1s), representing a population of young AGNs both with young jet and early accretion activity. The optical variabilities of 15 quasars with multi-epoch spectroscopy were investigated. Our results show that the optical variability in young AGN quasars presents low variations ($\leq 60\%$) similar to the normal radio-quiet quasars.

Key words: galaxies: active — accretion, accretion discs — galaxies: evolution — quasars: emission lines

1 INTRODUCTION

Young radio active galactic nuclei (AGNs) are a subclass of AGNs characterized by an intrinsically compact radio morphology and a peaked radio spectrum, including Gigahertz Peaked Spectrum (GPS) radio sources, Compact Steep Spectrum (CSS) radio sources and High Frequency Peaker (HFP) radio sources. The peak frequency in radio spectrum are around 1 GHz, 100 MHz, and above 5 GHz for GPS, CSS and HFP, respectively. Both GPS and HFP sources are with linear size (LS) below 1kpc, while CSS sources are well confined within 20kpc (O’Dea 1998). These radio AGNs are identified in both galaxies and quasars, with galaxies being at lower redshift, less variable than quasars and have symmetric radio morphologies, while quasars are detected at both low and high redshifts

and show core-jet structures (O’Dea 1998). It is usually believed that these radio sources will perhaps eventually evolve into large-scale radio sources, known as Fanaroff-Riley (FR) I and FR II sources based on the youth scenario (O’Dea 1998; Polatidis & Conway 2003; Randall et al. 2011), which is strongly supported by the measurements of dynamical and spectral age, about $10^3 - 10^5$ years (Owsianik et al. 1998; Murgia 2003; Polatidis & Conway 2003; Giroletti & Polatidis 2009; An et al. 2012). Therefore, they are important to study the triggering of radio/accretion activity and evolution of AGN as well as the relationship between the accretion and jet.

While many works have focused on radio investigations of young radio AGNs, their optical properties have not been sufficiently studied and there are only a few studies on various samples of young radio AGNs. Wu (2009) investigated the optical properties of a sample of 65 young radio galaxies (both GPS and CSS sources) based on the data collected from the literature. They found that most

★ E-mail: liaomai@shao.ac.cn

† E-mail: gumf@shao.ac.cn

young radio AGNs have relatively small black hole (BH) masses and high Eddington ratios which are similar to those of Narrow-line Seyfert 1 galaxies (NLS1s). [Son et al. \(2012\)](#) compiled a sample of 34 low-redshift young radio galaxies including high-excitation galaxies (HEGs) and low-excitation galaxies (LEGs) to study their accretion properties. The BH mass distribution was found to be similar to large-scale radio galaxies, while accretion activity presented a diversity. While these two works give us clues on the accretion process in young radio AGNs, the source number in their sample is rather limited. A larger sample is needed to further systematically study the optical properties of young radio AGNs, especially the combination of the radio and optical properties will give clues on the AGN evolution and jet-disk relation.

NLS1s are a special class of AGNs. It is well known that they have smaller black hole masses and higher accretion rates compared to typical broad-line AGNs, suggesting that NLS1s are candidates of young AGNs and may be in the early stage of AGN accretion activity ([Komossa 2008](#)). Recent works show that some radio-loud NLS1s are CSS-like sources and they share same radio properties with young radio AGNs ([Komossa et al. 2006](#); [Gu & Chen 2010](#); [Caccianiga et al. 2014](#); [Gu et al. 2015](#)). These objects may represent an AGN population with both jet and accretion activity at early stage of evolution. Searching for NLS1s in the sample of young radio AGNs enables us to find more targets, and then to investigate the jet and accretion, their relation, and AGN evolution in general.

In this work, our goal is to systematically study accretion properties, evolution in young radio AGNs and to search for NLS1s candidates by analyzing the SDSS spectra of a larger sample. In addition we will study stellar velocity dispersion versus gas velocity dispersion, jet-disk relation and optical variability. Section 2 presents the details of sample selection. The spectral analysis is shown in Section 3, in which the measurements of emission lines and stellar velocity dispersions are given. In Section 4, we show the main results. Section 5 gives discussions and the main results are summarized in Section 6. Throughout this paper, the cosmological parameters $H_0 = 70 \text{ km s}^{-1} \text{ Mpc}^{-1}$, $\Omega_m = 0.3$, and $\Omega_\lambda = 0.7$ is adopted. The spectral index α_λ is defined as $f_\lambda \propto \lambda^{\alpha_\lambda}$ with f_λ being the flux density at wavelength λ .

2 SAMPLE SELECTION

To systematically study the optical properties of the largest possible sample of young radio AGNs, we firstly collected all available radio-selected samples of young radio AGNs in the literature. Besides GPS, CSS and HFP sources, the Compact Symmetric Objects (CSO) are also included in our sample, which are also believed to be young AGNs, and share similar properties as GPS radio galaxies ([O’Dea 1998](#)). The source classification (i.e., CSS/GPS/HFP/CSO) is directly taken from the literature based on radio properties (e.g., radio size, spectral shape and peak frequency, and/or radio morphology).

The CSS sources were collected from [Spencer et al. \(1989\)](#), [Fanti et al. \(1990\)](#) (3C and PW catalogue combined), [Fanti et al. \(2001\)](#) (B3/VLA sample), [Kunert et al. \(2002\)](#) (the FIRST sample), [Edwards & Tingay \(2004\)](#)

(ATCA sample), [Snellen et al. \(2004\)](#) (the CORALZ sample) and [Kunert-Bajraszewska et al. \(2010\)](#). For GPS sources, the radio-selected samples of [Stanghellini et al. \(1998\)](#) (1-Jansky catalogues), [Snellen et al. \(1998\)](#) (faint WENSS sample), [Snellen et al. \(2002\)](#) (Parkes 0.5 Jy sample), [Edwards & Tingay \(2004\)](#) (ATCA sample) and [Snellen et al. \(2004\)](#) (the CORALZ sample) were included. We collected HFP sources from [Dallacasa et al. \(2000\)](#) and [Stanghellini et al. \(2009\)](#), and CSO sources from [Peck & Taylor \(2000\)](#) (COINS sample), [Snellen et al. \(2004\)](#) (the CORALZ sample), and [An & Baan \(2012\)](#). This selection produces a sample of 250 CSS, 148 GPS, 116 HFP, and 80 CSO radio sources. After removing the overlap sources in the literature, the sample consists of 545 radio sources, which is the parent sample of our study.

Then, we searched for the SDSS spectroscopic counterparts of the young radio AGNs within 2 arcsec from the NED position¹ for all the objects in parent sample. This results in our optical sample, consisting of 147 sources.

2.1 Excluding blazar-type objects

It is generally believed that young radio AGNs have the least variability in the total flux density when compared with flat-spectrum radio sources ([O’Dea 1998](#)). Moreover, GPS and CSS quasars are not as strongly beamed as the core-dominated quasars because the optical polarization of GPS/CSS radio sources are very low in comparison to core-dominated quasars ([O’Dea 1998](#)). However, it should be noticed that a large portion of these sources studied in the literature have limited radio data and they may be contaminated by blazars, which can be temporarily inverted in their radio spectrum. Simultaneous long-term radio observations at several frequencies are needed to search genuine GPS and HFP radio sources.

The source nature of HFP/GPS sources has been explored in various works. [Oriente et al. \(2007\)](#) and [Oriente & Dallacasa \(2008\)](#) carried out simultaneous multi-frequency VLA observations to investigate the variability and polarization properties of bright HFPs in [Dallacasa et al. \(2000\)](#). [Oriente et al. \(2010\)](#) and [Oriente & Dallacasa \(2012\)](#) studied the variability and morphology of faint HFPs in [Stanghellini et al. \(2009\)](#), while systematic multi-frequency studies of GPS radio sources were shown in [Mingaliev et al. \(2012\)](#). We checked the GPS and HFP objects of our parent and optical sample with these works. We find 77 (14 %) objects out of the parent sample and 21 (14 %) sources in optical sample show significant flux density and spectral variability, or do not preserve the convex spectrum all the time with flat radio spectrum at various epochs. These sources are most likely blazar-type sources and should be excluded when studying genuine young radio AGNs properties.

2.2 Final sample

After removing the blazar-type sources from the parent and optical sample, it results in 468 and 126 sources in final parent and optical sample, respectively.

¹ <http://ned.ipac.caltech.edu>

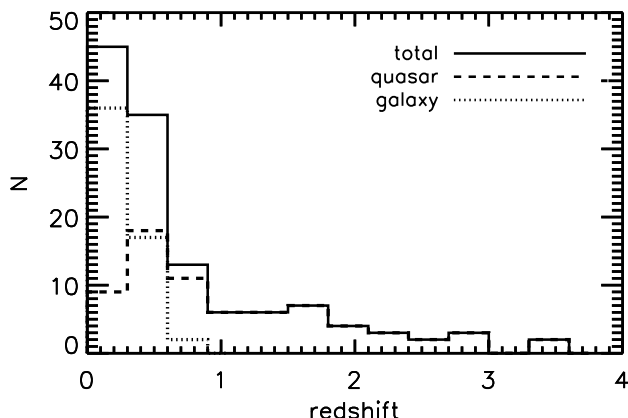


Figure 1. The redshift distribution of our sample. The dotted, dashed and solid lines represent galaxies, quasars and whole sample, respectively.

The detailed information of the final optical sample are presented in Table 1, including 82 CSS, 19 GPS, 19 HFP and 6 CSO for 71 QSOs and 55 galaxies according to SDSS classification. We retained all spectra for those objects with multiple spectroscopic observations in order to analyse their optical variability, but only the spectrum with highest median signal-to-noise ratio (S/N) was used in sample statistical analysis, which is listed in Table 1.

The redshift distribution of our sample is shown in Figure 1, from which the redshift of galaxies range from 0.025 to 0.730, and quasars cover broad range of 0.077 – 3.594.

2.3 Two additional GPS sources

Many young radio AGNs do not have optical spectral data in SDSS or other archives. In order to increase available spectrum, we observed two GPS sources HB89 1127–145 and CGRaBS J1424+2256 on May 11 and 12, 2012, respectively, by using the Yunnan Faint Object Spectrograph Camera (YFOSC) installed on Lijiang 2.4m telescope at Yunnan Observatory (Bai & Liu 2010), Chinese Academy of Sciences. Two objects were observed by using G8 grating with a dispersion of $1.5 \text{ \AA pixel}^{-1}$, and a wavelength coverage of 4970 – 9830 Å, and the exposure time is 1800 seconds for each target. The spectra were reduced in IRAF following standard process, including bias subtraction, flat field correction and cosmic ray removal. Neon and helium lamps were used for wavelength calibration. The spectra were flux calibrated using the standard stars observed on the same night. The spectra of two GPS sources are shown in Figure 2, from which Mg II, C IV and Ly α lines are clearly seen.

For this work, these two sources were not used in following statistic analysis to avoid systematic bias between Lijiang telescope and SDSS. We just presented the spectra information for HB89 1127–145 and CGRaBS J1424+2256, including the emission lines measurements (see details in Table 2), black hole mass and Eddington ratio estimation (see details in Table 1).

3 SPECTROSCOPIC ANALYSIS

The SDSS spectra were firstly corrected for Galactic extinction with the reddening map of Schlegel et al. (1998), and then were shifted to the rest-frame wavelength by using the redshift from the header of SDSS spectra. The spectra of galaxies and low-redshift quasars in our sample may be contaminated by the host galaxy starlight, which should be removed in order to study AGN emission. Firstly, we used the 4000 Å break index D_{4000} (defined as the flux ratio in 4000–4100 Å to 3850–3950 Å) introduced by Balogh et al. (1999) where $D_{4000} = \int_{4000}^{4100} f_{\lambda} d\lambda / \int_{3850}^{3950} f_{\lambda} d\lambda$, to evaluate the significance of stellar component. For those sources with $D_{4000} \leq 1$, the contribution of host galaxy can be ignored and the spectra is dominated by AGN nuclei (Dong et al. 2005; Wang & Wei 2009). In 55 galaxies, the D_{4000} of all but two sources are greater than 1, while it is the case in 16 out of 71 quasars.

In this work, we mainly focus on the measurements of emission lines, i.e., H α , H β , Mg II and C IV broad lines and [O III], [O II], [S II] narrow lines. To ensure the reliability of line measurements, we used the ratio of the integral line flux for the whole profile to the rms deviation around these lines to determine if the spectra is valuable to be analyzed for the lines, as some spectra have rather low S/N and the emission lines are not significant from visually inspection. The rms deviation were calculated by using the pixel-to-pixel deviation in the continuum-subtracted spectrum (see details in Section 3.1) in the spectral region surrounding the relevant lines. We found a significant correlation between the flux ratio and S/N for all our spectra. The median value of flux ratio is about 70 Å for the sources with S/N < 4. The sources above 70 Å thus correspond to those with S/N ≥ 4 in general. Tentatively in this work, the spectra with the flux ratio of all the focused lines to the rms deviation of the continuum below 70 Å were not further analyzed. There are 16 sources meeting the criterion², of which all have low-quality spectra with median S/N < 10 except for one objects.

According to S/N and D_{4000} , the remaining 110 young radio AGNs were divided into three groups:

- (A) 30 galaxies and 7 quasars, the spectra with S/N ≥ 10 and $D_{4000} > 1$;
- (B) 10 galaxies and 9 quasars, the spectra with S/N < 10 and $D_{4000} > 1$;
- (C) 53 quasars and 1 galaxy, the spectra with $D_{4000} \leq 1$.

3.1 Continuum subtraction

The continuum was fitted differently depending on the significance of host galaxy and S/N. Due to the significant host contribution in the spectra of group A sources, we used the direct-pixel-fitting code Penalized Pixel-Fitting (PPXF) of Cappellari & Emsellem (2004) and Cappellari (2017) to fit the continuum and measure the stellar velocity dispersions σ_* . We focused on the spectral range of 3540 – 6900 Å, which covers absorption lines Ca H+K, and Mg b

² We retained the spectra of SDSS J082504.56+315957.0 and SDSS J120902.79+411559.2 due to the $D_{4000} > 1$ and SN > 10. We can measure the σ_* for the spectra.

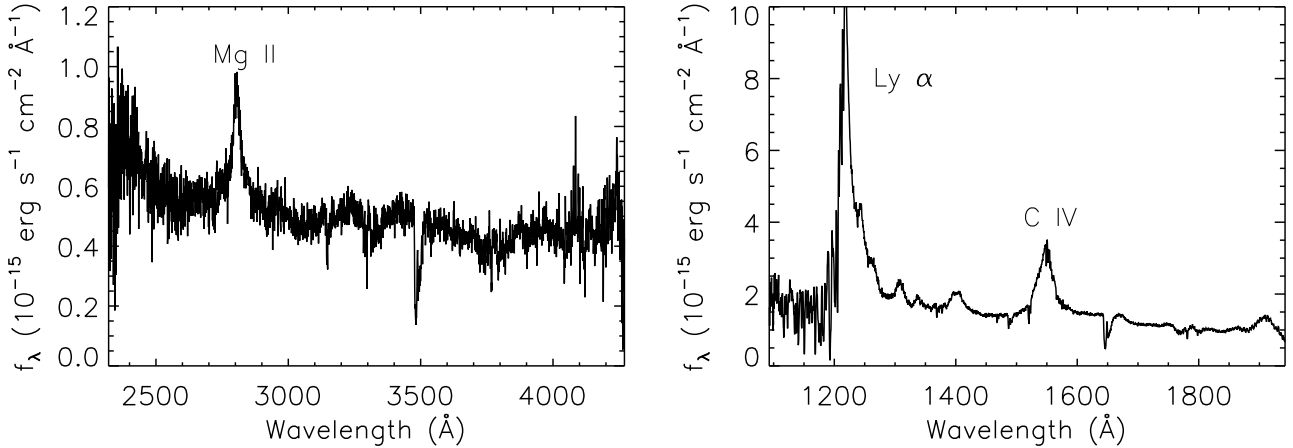


Figure 2. The spectra of HB89 1127-145 (*left*) and CGRaBS J1424+2256 (*right*) observed using Lijiang 2.4m Telescope. Two spectra were corrected for Galactic extinction and shifted to source rest-frame, with main emission lines indicated.

triplet. The emission lines were masked out before the fitting. A linear combination of 156 single stellar population (SSP) templates (Vazdekis et al. 2010) from MILES library (Sánchez-Blázquez et al. 2006) with a broadening by line-of-sight velocity distribution (LOSVD) was applied by performing a χ^2 minimization. The stellar templates give good fit to the spectra (see example in Figure 3) for all sources, when adding a low-order Legendre polynomial on the continuum (e.g., Son et al. 2012).

Due to low S/N in group B and its resulting large uncertainties in extracting host component, we simply fitted the continuum around individual emission lines with a single power-law.

For 54 sources in group C, the continuum is dominated by AGN emission. Therefore, a single power-law and Fe II emission, were applied to fit local continuum for H α , H β , Mg II (see Figure 4), with the fitting windows similar to Shen et al. (2011). In general, Fe II lines are very weak nearby C IV, therefore, only a single power-law was employed to fit C IV, as did in Shen et al. (2011).

3.2 Emission line measurements

We fitted the emission lines using Gaussian profiles on the continuum-subtracted spectra. All the narrow line components of H α , [N II] $\lambda\lambda$ 6548,6584, [S II] $\lambda\lambda$ 6716,6731, H β , [O II] λ 3727 and Mg II were modelled with a single Gaussian component. The [O III] $\lambda\lambda$ 4959,5007 were fitted using one or double Gaussian profiles, when necessary in cases of complex shapes, i.e., asymmetric blue or red wings. The broad components of H α , H β , and Mg II were fitted with one or multiple Gaussian profiles (up to three). We fitted C IV with three broad Gaussians following Shen et al. (2011) despite some attempts also considered the narrow component in the literature (Bachev et al. 2004; Sulentic et al. 2007). We imposed an upper (lower) limit on the line width of narrow (broad) components with $\text{FWHM} < 1000 \text{ km s}^{-1}$ ($\geq 1000 \text{ km s}^{-1}$).

In this work, the line region of H α and H β , Mg II and C IV were fitted individually. The line width and offset of narrow lines H α , and [N II] $\lambda\lambda$ 6548,6584 were constrained to be same. The same treatments were applied for narrow H β and the line core of [O III] $\lambda\lambda$ 4959,5007. The line width and offset of [S II] $\lambda\lambda$ 6716,6731 were tied to each other. The

flux ratio of [N II] doublet was fixed to be 2.96 and [O III] doublet was constrained to be 3 (Shen et al. 2011).

The χ^2 -minimization was used to obtain the best fit for the continuum and emission lines. To estimate the errors in the measured quantities, we generated 100 mock spectra by adding a random Gaussian noise to original spectra using the flux density errors, and then estimated the uncertainty as the standard deviation of measurements from those mock spectra. The examples of spectral fitting are presented in Figure 3 and Figure 4. The measured flux and line width of studied emission lines are displayed in Table 2. All the widths of the narrow lines were corrected by the instrumental resolution of SDSS using equation of

$$\text{FWHM}_{\text{intrinsic}} = \sqrt{\text{FWHM}_{\text{observed}}^2 - \text{FWHM}_{\text{instrumental}}^2}$$

As mentioned earlier, the spectral fitting was carried out for 110 out of 126 young radio AGNs, consisting of 69 quasars and 41 galaxies. Our spectral analysis shows that 57 quasars have broad emission lines ($\text{FWHM} \geq 1000 \text{ km s}^{-1}$)³, while only narrow emission lines were detected in the remaining 12 quasars, of which three objects have σ_* measurements (i.e., SDSS J102844.26+384436.8, SDSS J140942.44+360415.9, and SDSS J161148.52+404020.9). In comparison, the broad emission lines were found in two galaxies (i.e., SDSS J090615.53+463619.0 and SDSS J160246.39+524358.3).

4 RESULTS

4.1 Narrow lines versus σ_*

It is well known that there is a close correlation between the BH mass and the stellar velocity dispersion (σ_*) of the bulge in nearby normal galaxies. This relation is a key to understand the formation and evolution of galaxies (Ferrarese & Merritt 2000; Tremaine et al. 2002; Kormendy & Ho 2013; McConnell & Ma 2013). However, usually σ_* is difficult to measure in bright AGNs, and thus the line width of narrow line [OIII] was frequently used as a

³ It should be noticed that our definition of broad line is stricter than that of SDSS classification, i.e., any lines with $\text{FWHM} > 500 \text{ km s}^{-1}$

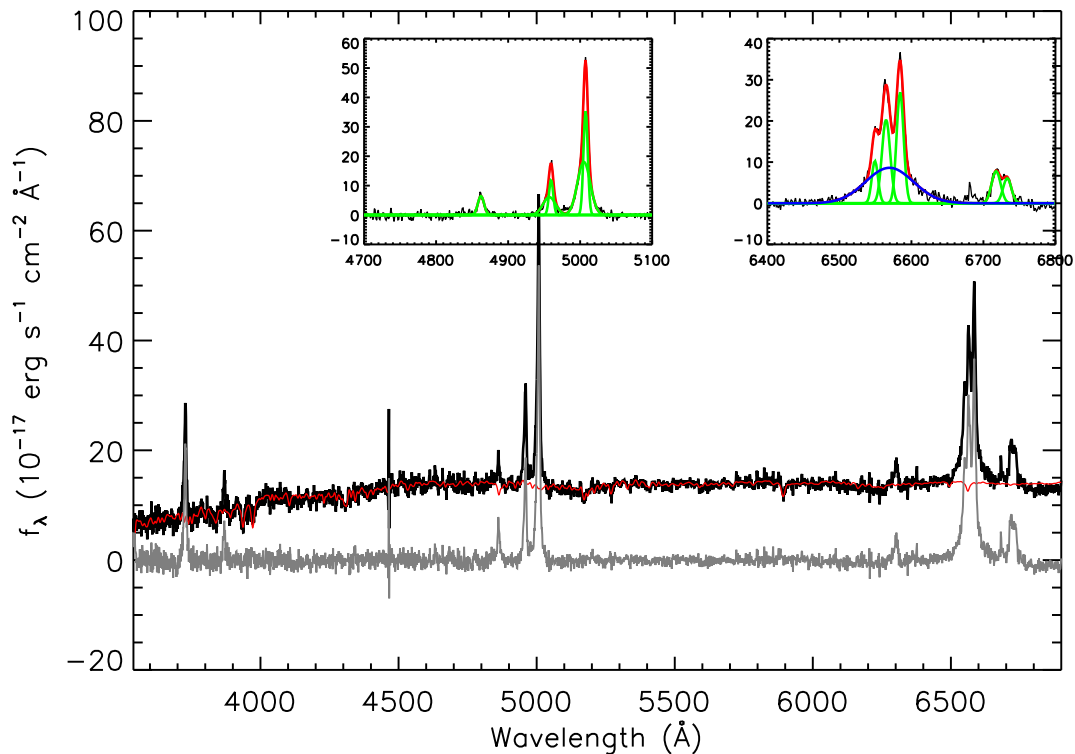


Figure 3. The spectral fitting of SDSS J124419.96+405136.8 ($z = 0.249$) as an example of source in group A, where the significant contribution of host galaxy on the continuum was fitted using PPXF. The black and grey lines are the original and the continuum-subtracted spectra, respectively. The red line is the fitted continuum. The two insets represent the spectral fitting around $H\alpha$ and $H\beta$ lines. The blue, green, and red lines are the fitted broad, narrow and total components, respectively.

surrogate for σ_* because the gravity of bulge dominates the global kinematics of Narrow Line Region (NLR) in AGNs (Nelson & Whittle 1996; Boroson 2003; Greene & Ho 2005; Komossa & Xu 2007). The $\sigma_{[\text{O III}]}$ has been commonly used as a surrogate for the σ_* of host bulge in AGNs after removing wing component and there is a strong relationship between them. (Komossa & Xu 2007; Xiao et al. 2011; Cracco et al. 2016). This can be tested for our sample when both σ_* and $[\text{O III}]\lambda 5007$ line width are directly measured.

We only considered those spectra with high S/N ≥ 10 , and line width measurements of $[\text{O III}]$ and $[\text{S II}]$ at high significance ($> 3\sigma$). The relationship between the stellar velocity dispersion (σ_*) and the velocity dispersion of $[\text{O III}]$ line core ($\sigma_{[\text{O III}]} = \text{FWHM}_{[\text{O III}]} / 2.35$), and $[\text{S II}]$ velocity dispersion ($\sigma_{[\text{S II}]} = \text{FWHM}_{[\text{S II}]} / 2.35$) are shown in Figure 5. The correlation analyses show that the velocity dispersion of $[\text{O III}]$ core component has a strong correlation with σ_* for 33 sources, with a Spearman rank correlation coefficient $r_s = 0.65$ and the probability P_{null} less than 10^{-4} for the null hypothesis of no correlation, while σ_* correlates less strongly with velocity dispersion of $[\text{S II}]$ ($r_s = 0.38$, $P_{\text{null}} = 0.03$) for 33 objects. This suggests that $[\text{O III}]$ can be a better surrogate than $[\text{S II}]$ at least in our sample of young radio AGNs, which is supported by the mean values of -0.002 ± 0.110 , and 0.035 ± 0.120 for $\log(\sigma_{[\text{O III}]} / \sigma_*)$, and $\log(\sigma_{[\text{S II}]} / \sigma_*)$, respectively (see right panels in Figure 5).

In our work, the strong blueshifted wing of $[\text{O III}]$ was found in young radio AGNs and the width of $[\text{O III}]$ tends to be broad (Gelderman & Whittle 1994; O’Dea et al. 2002;

Holt et al. 2008; Kim et al. 2013). Such blueshifted/broad wing may be caused by the outflow or the strong interaction between jet and ambient gas or ISM when jet expands outward (Labiano 2008). Our results show that 15 out of 68 sources with $[\text{O III}]$ measurements present blueshifted wing. We find that the line width of $[\text{O III}]$ core strongly correlates with σ_* , indicating it can be well used as a surrogate of σ_* in young radio AGNs. Therefore, we can derive the σ_* from the width of core component of $[\text{O III}]$ ($\sigma_* = \text{FWHM}_{[\text{O III}]} / 2.35$) if there is no σ_* measurement for the type 2 sources in our sample, to estimate their black hole mass.

However, large scatter and deviation from the equivalent line are clearly seen at $\sigma_{[\text{O III}]} > 300 \text{ km s}^{-1}$. Such broad line width could be related with jet–ISM interaction (e.g., Kim et al. 2013). In principle, $[\text{S II}]$ should be a better surrogate of σ_* than $[\text{O III}]$ because the latter may suffer from outflow/interaction. However, we found a weaker relationship between the width of $[\text{S II}]$ and σ_* than $\sigma_{[\text{O III}]} - \sigma_*$ relation, not as expected. This may at least partly be caused by the asymmetric $[\text{S II}]$ profile found in many of our sources, however is not fully fit in our single-Gaussian spectral fitting. Although the details are unknown, the asymmetric profile is most likely caused by the interaction between jet and ambient medium, similarly as $[\text{O III}]$ but less significant.

4.2 Black hole mass and Eddington Ratio

The black hole mass and Eddington ratio are two fundamental parameters in AGN studies, which can be used to

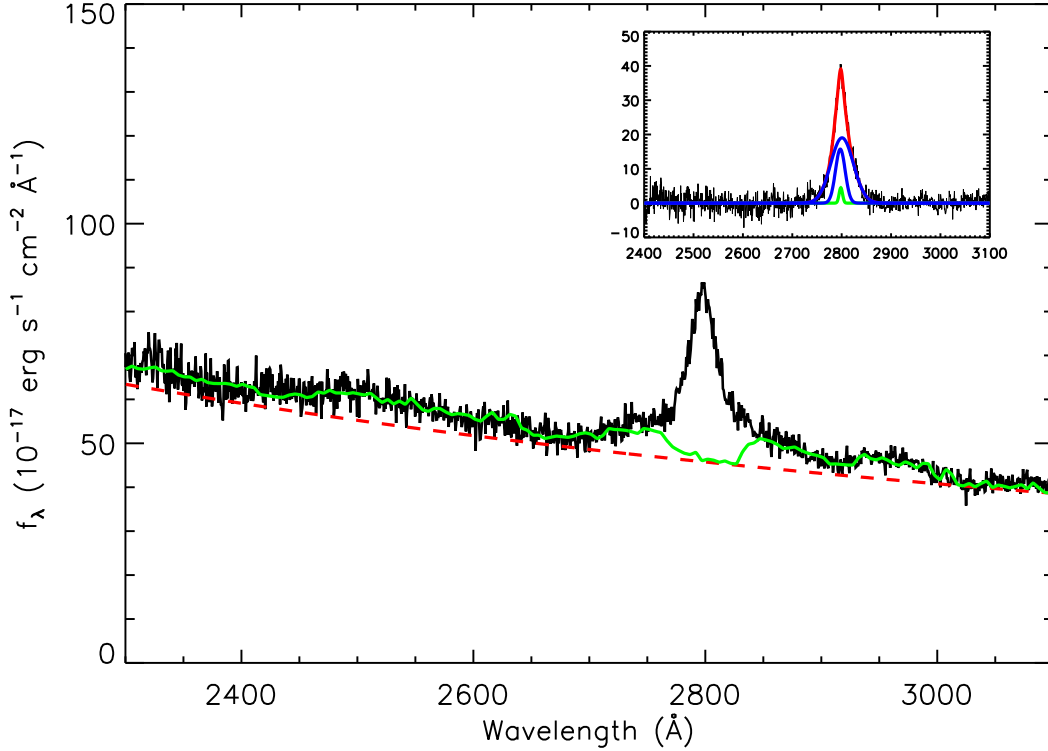


Figure 4. The spectral fitting of SDSS J005905.51+000651.6 ($z=0.719$) as an example of source in group C, where the AGN emission is dominant and the continuum is fitted with a single power-law and Fe II emission. The black line is the original spectrum. The power-law and total fitted continuum including Fe II emission are shown with the red dashed and green lines, respectively. The inset shows the line fitting for Mg II. Lines and symbols as in Figure 3.

study the accretion mode (e.g., advection-dominated accretion flow or standard accretion disc), and the source position in AGN evolution (e.g., NLS1s) (Komossa et al. 2006).

4.2.1 Black hole mass estimation

Young radio AGNs are radio-loud sources, therefore their optical continuum emission may be more or less affected by the synchrotron emission from jets (e.g., in GPS and HFP) (Baker & Hunstead 1995). This can be studied by directly comparing the relationship between the continuum luminosity and the broad emission line luminosity in our sources with that of radio-quiet AGNs, in which the relativistic jets are absent or weak. The comparisons are shown in Figure 6 for L_{5100} and $L_{H\beta}$, L_{3000} and L_{MgII} , and L_{1350} and L_{CIV} , with the data of radio-quiet AGNs taken from the literature (Vestergaard & Peterson 2006; Kong et al. 2006). The dashed lines in Figure 6 show the linear fit to the relation between continuum luminosity to line luminosity for radio-quiet AGNs. While radio-quiet quasars distribute tightly around the line, our young radio AGNs show a large scatter with most objects below the line. This indicates that the continuum luminosity of our sample is larger than that of radio-quiet AGNs at the fixed emission line luminosity, and the deviation can even be larger than 0.5 dex in some cases. The K-S test was also applied to check whether the difference between the continuum and line luminosity is significant or not. The test results show that the difference is significant with P-value of 0.01, 0.001, 0.002 for the ratios of

line-to-continuum luminosity in $L_{H\beta}/L_{5100}$, L_{MgII}/L_{3000} and L_{CIV}/L_{1350} between our and radio-quiet sources, respectively, implying that the continuum emission is likely contaminated by the jet emission in our sample.

Due to the likely presence of jet emission in the continuum, we used the line width and luminosity of various broad emission lines to calculate the black hole mass instead of continuum luminosity in order to avoid overestimation. The empirical relations used for $H\alpha$ and $H\beta$ (Greene & Ho 2005; Vestergaard & Peterson 2006), and Mg II and C IV (Kong et al. 2006) are as following:

$$M_{BH} = 1.3 \times 10^6 \left(\frac{L_{H\alpha}}{10^{42} \text{ ergs s}^{-1}} \right)^{0.57} \left(\frac{FWHM_{H\alpha}}{10^3 \text{ km s}^{-1}} \right)^{2.06} M_{\odot} \quad (1)$$

$$M_{BH} = 4.7 \times 10^6 \left(\frac{L_{H\beta}}{10^{42} \text{ ergs s}^{-1}} \right)^{0.63} \left(\frac{FWHM_{H\beta}}{10^3 \text{ km s}^{-1}} \right)^2 M_{\odot} \quad (2)$$

$$M_{BH} = 2.9 \times 10^6 \left(\frac{L_{MgII}}{10^{42} \text{ ergs s}^{-1}} \right)^{0.57} \left(\frac{FWHM_{MgII}}{10^3 \text{ km s}^{-1}} \right)^2 M_{\odot} \quad (3)$$

$$M_{BH} = 4.6 \times 10^5 \left(\frac{L_{CIV}}{10^{42} \text{ ergs s}^{-1}} \right)^{0.60} \left(\frac{FWHM_{CIV}}{10^3 \text{ km s}^{-1}} \right)^2 M_{\odot} \quad (4)$$

Due to the torus obscuration (Son 2012, Berton 2015) (see details panel (4) in Figure 7 of BH mass comparison

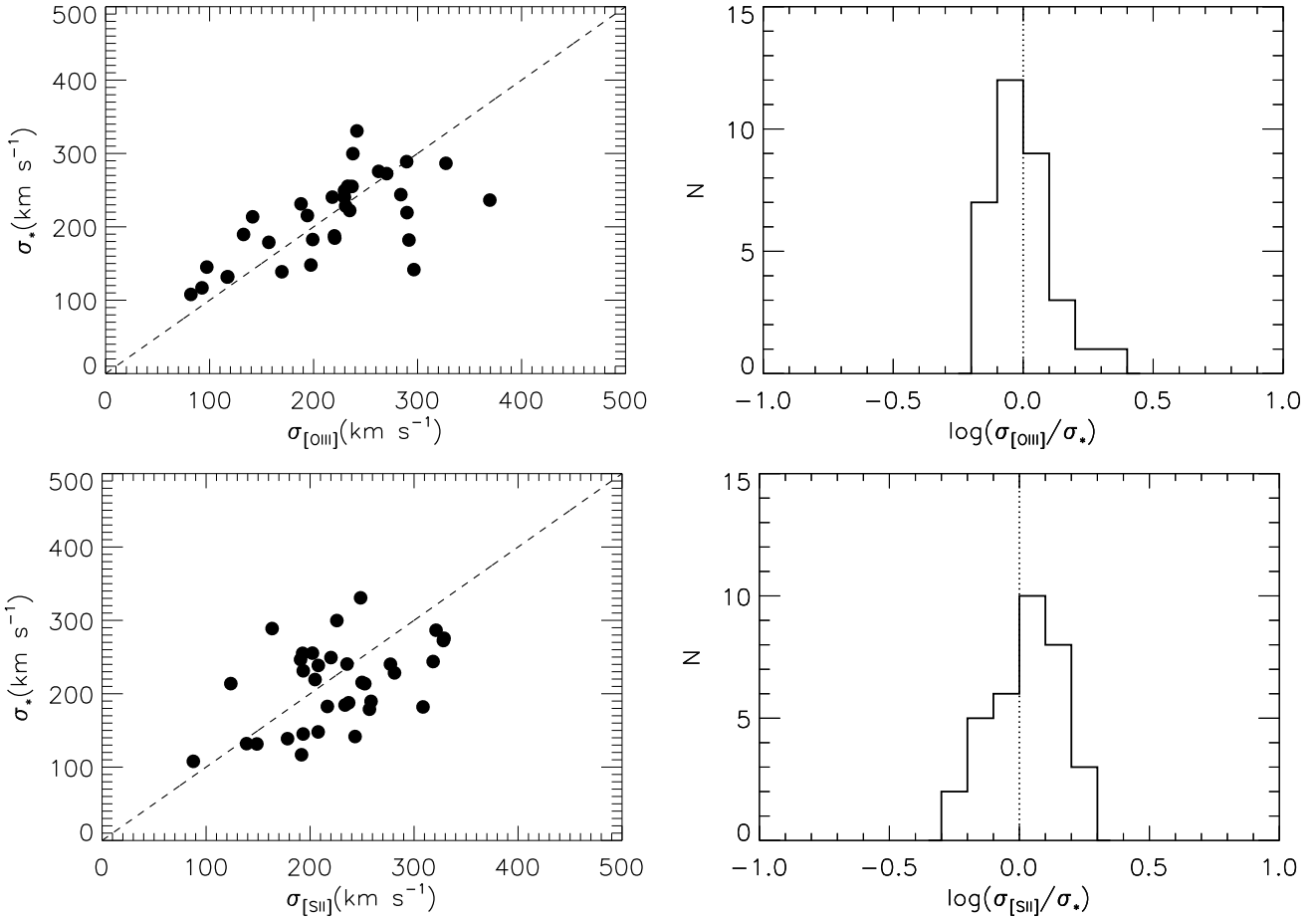


Figure 5. σ_* and narrow lines: *upper left*– σ_* versus $\sigma_{[\text{O III}]} = \text{FWHM}_{[\text{O III}]} / 2.35$ of [O III] core component; *upper right*– Histogram of $\log(\sigma_{[\text{O III}]} / \sigma_*)$; *lower left*– σ_* versus $\sigma_{[\text{S II}]} = \text{FWHM}_{[\text{S II}]} / 2.35$; *lower right*– Histogram of $\log(\sigma_{[\text{S II}]} / \sigma_*)$. Dashed lines represent the 1:1 relation. The dotted vertical lines mark the mean value of zero.

between broad H α and σ_* with more than one order of magnitude difference in median values), we preferred to use σ_* with the relation of $M_{\text{BH}} - \sigma_*$ in Kormendy & Ho (2013) to get the black hole mass for the sources both with broad line and σ_* measurements:

$$\log\left(\frac{M_{\text{BH}}}{M_{\odot}}\right) = 8.49 + 4.38 \times \log\left(\frac{\sigma_*}{200 \text{ km s}^{-1}}\right) \quad (5)$$

For the sources without significant stellar absorption but with broad lines, we used the broad lines to estimate the BH mass (empirical relations (1)-(4)). In this situation, when more than one broad line is available in the source, we preferred a priority sequence of H β (H α), Mg II, C IV to estimate the black hole mass. In the sources with only [O III] $\lambda 5007$ line core available, we estimated the BH masses using the width of [O III] line core.

The method used to estimate the black hole mass for each source is listed in Column 11 of Table 1.

We investigated for the sources with both broad lines and σ_* , or both broad lines and [O III] lines, or various broad lines simultaneously (C IV and Mg II, Mg II and H β , H β and H α) to check the consistence of black hole masses estimation. Our results in Figure 7 show that the median values of black hole mass estimation from various methods are generally consistent with each other within the typical uncertainty of 0.5 dex except for broad H α - σ_* , support-

ing broadly consistent results when using different methods. However, we noticed that the black hole masses estimated from C IV are systematically lower than those from Mg II, which is apparently different from Mg II - H β comparison. Indeed, the median values of $\log(M_{\text{BH}}^{\text{Mg II}} / M_{\text{BH}}^{\text{C IV}})$ and $\log(M_{\text{BH}}^{\text{H}\beta} / M_{\text{BH}}^{\text{Mg II}})$ are 0.42 dex and 0.03 dex, respectively. This may be related with the non-virialized component, usually blueshifts in C IV line, as suggested in Shen et al. (2008). The authors found that $\log(M_{\text{BH}}^{\text{Mg II}} / M_{\text{BH}}^{\text{C IV}})$ is correlated with the C IV - Mg II blueshift, and the C IV estimator tends to give smaller virial masses than the Mg II estimator for objects with small blueshifts (≤ 1000 km/s) but larger C IV masses for larger blueshifts. Consistently, we found that the available C IV - Mg II blueshifts in six of our sources from Shen et al. (2008) are around or less than 1000 km/s. While this effect may cause the uncertainty in C IV-based mass, the median value of C IV - Mg II mass difference is less than typical uncertainty of 0.5 dex. Moreover, the black hole masses are only estimated in eight sources using C IV line in our sample. Therefore, our conclusion will not be altered considering the small source fraction and generally consistent C IV - Mg II mass estimations.

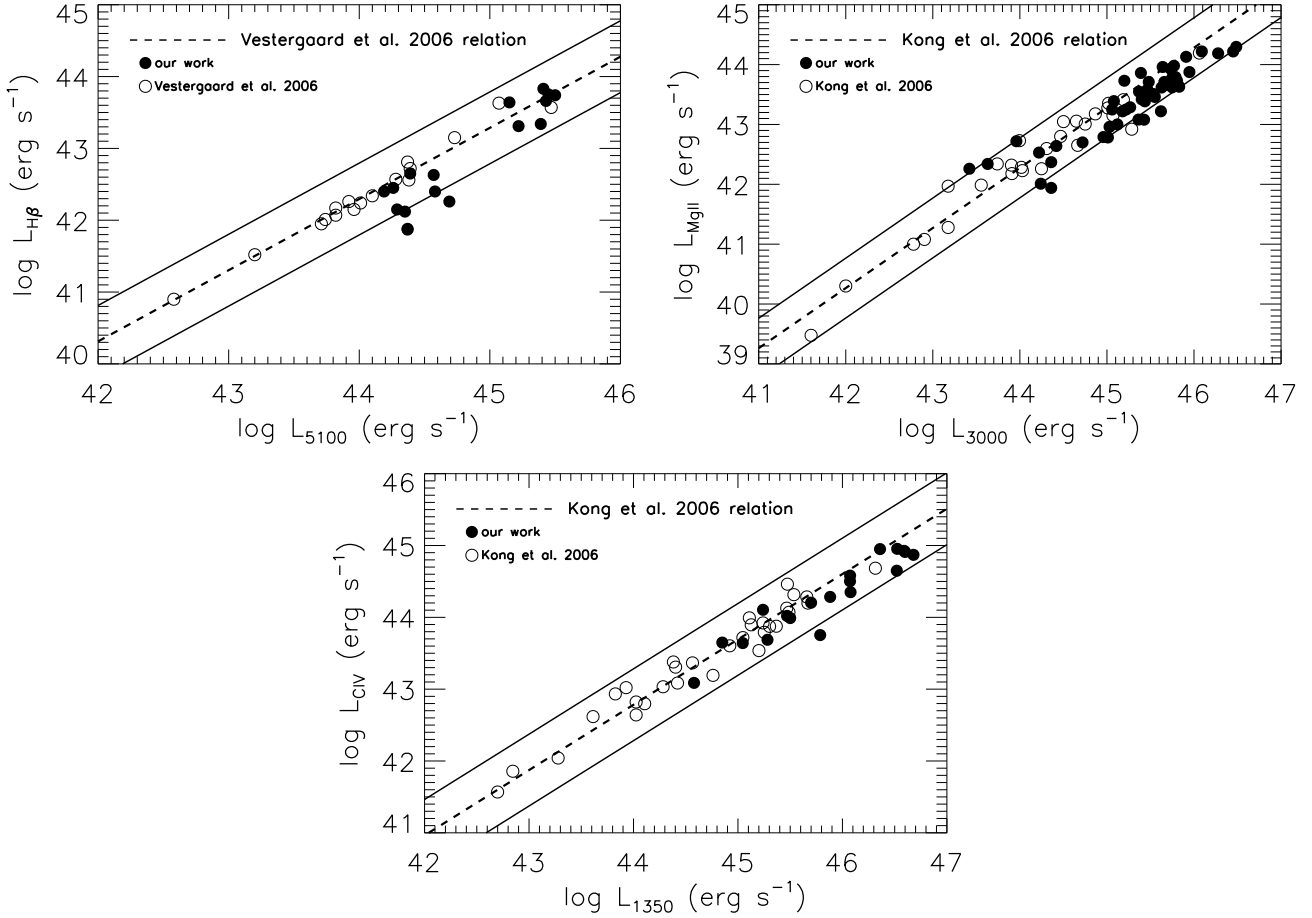


Figure 6. The luminosities of broad H β , Mg II, and C IV versus the continuum luminosities at 5100 Å, 3000 Å, and 1350 Å, respectively. The filled circles are the sources in our work, while open circles denote the radio-quiet quasars in the literature. The dashed lines represent the linear fit between the continuum and broad line luminosities for radio-quiet quasars in the literature. The solid lines show 0.5 dex deviation from the dashed lines.

4.2.2 Eddington ratio estimation

We calculated the bolometric luminosity assuming $L_{\text{bol}} = 10L_{\text{BLR}}$ (e.g., Liu et al. 2006) for AGNs with broad line measurements, where L_{BLR} is the luminosity of broad line region. L_{BLR} was estimated following the method of Celotti et al. (1997) by scaling the strong broad emission lines H α , H β , Mg II and C IV to the quasar template spectrum of Francis et al. (1991), where Ly α is used as a reference of 100. The total relative BLR flux is 555.77, and H α , H β , Mg II and C IV are 77, 22, 34, and 63, respectively (Francis et al. 1991; Celotti et al. 1997). For example, when H β and Mg II are available, we calculated the bolometric luminosity using the relation $L_{\text{bol}} = 10 \times 555.77 \times (L_{\text{H}\beta} + L_{\text{MgII}})/(22 + 34)$. For those AGNs without broad line measurements, we estimated the bolometric luminosity from [O III] line by using the relationship between two parameters. Following Berton et al. (2015), we constructed a self-consistent relation $L_{\text{bol}} - L_{[\text{OIII}]}$ from the sources having both broad lines and [O III] line in our sample. The $L_{\text{bol}} - L_{[\text{OIII}]}$ relation is shown in Figure 8 as

$$\log \left(\frac{L_{\text{bol}}}{\text{erg s}^{-1}} \right) = (10.01 \pm 4.8) + (0.82 \pm 0.11) \log \left(\frac{L_{[\text{OIII}]}}{\text{erg s}^{-1}} \right). \quad (6)$$

It is in good agreement with that of Berton et al. (2015). Our relation is then used to estimate L_{bol} , similarly as the relation of Berton et al. (2015) used for CSS sources in Berton et al. (2016).

By using the black hole mass and bolometric luminosity, the Eddington ratio $R_{\text{edd}} = L_{\text{bol}}/L_{\text{edd}}$ can be calculated where $L_{\text{edd}} = 1.38 \times 10^{38} M_{\text{BH}}/M_{\odot} \text{ erg s}^{-1}$.

4.2.3 Black hole mass and Eddington ratio distributions

In our sample, we were able to estimate BH masses for 106 sources (69 quasars and 37 galaxies), and Eddington ratios for 69 quasars and 33 out of 37 galaxies since four galaxies have no broad line nor [O III] line measurements. The distribution of BH masses and Eddington ratios are shown in Figure 9. We find that the BH masses (M_{BH}) have a distribution ranging from $10^{7.32}$ to $10^{9.84} M_{\odot}$ with a peak around $10^9 M_{\odot}$ and a median value of $10^{8.72} M_{\odot}$. In Figure 9, it seems that galaxies have on average larger masses than quasars. The average values of $\log M_{\text{BH}}$ are 8.61 and 8.73 for quasars and galaxies, respectively. This difference is further checked with K-S test, showing a significant difference in M_{BH} distributions between galaxies and quasars with P-value of 0.039. This difference in BH mass distribution is also found between large samples of quasars in Shen et al.

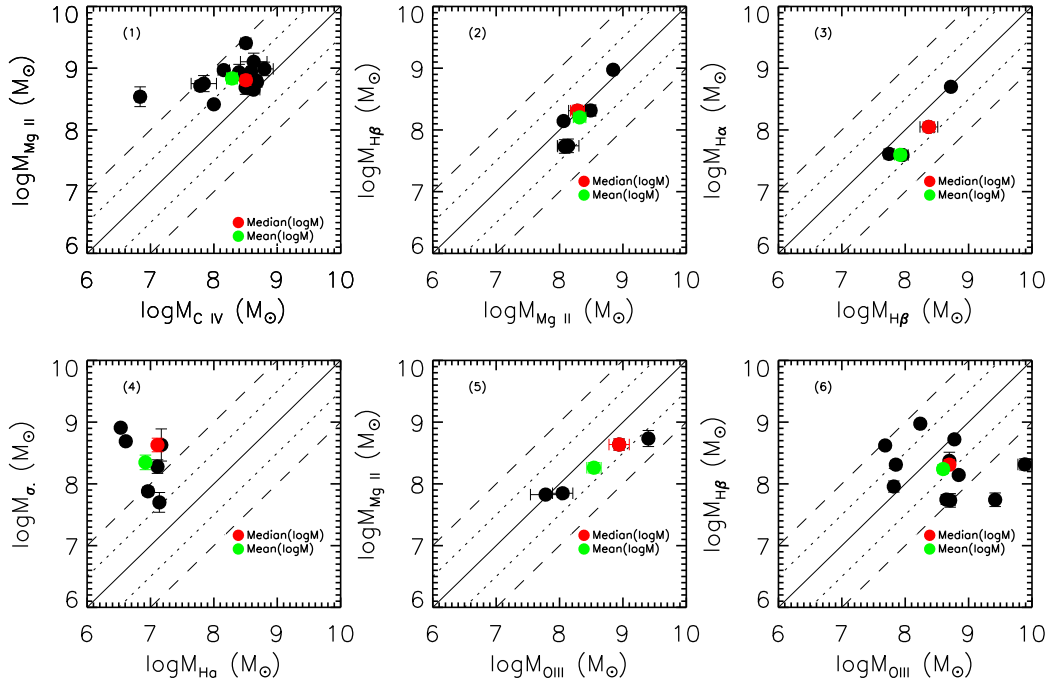


Figure 7. Black hole mass comparisons between various broad lines, or between broad line and σ_* , or between broad lines and [O III] lines. The red circles and the green circles are median value and mean value, respectively. Solid lines represent the 1:1 relation. The dotted lines and the dashed lines show 0.5 dex and 1 dex deviation from the solid lines, respectively.

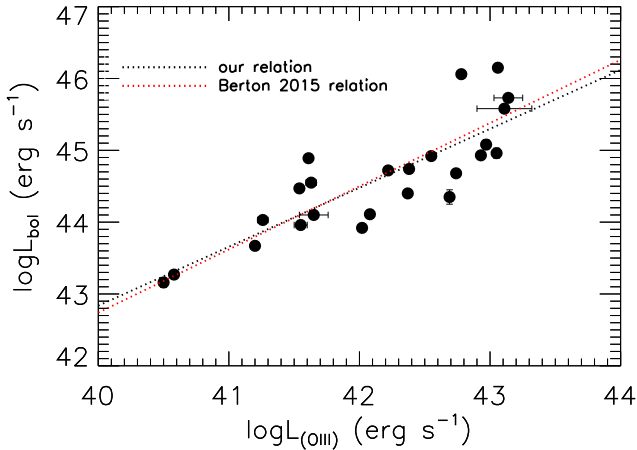


Figure 8. The relation between the luminosity of [O III] $\lambda 5007$ and the bolometric luminosity derived from broad lines. The black dashed line is the best fit, and the red dashed line is the relation from Berton et al. (2015).

(2011) and galaxies in Best et al. (2005) when using same methods to estimate the BH mass as in our work. The average values of $\log M_{\text{BH}}$ are 8.71 and 8.88 for the radio-loud quasars and galaxies, respectively, and the difference is confirmed with P-value of 0.036 from K-S test. The Eddington ratios R_{edd} have a wide distribution that range from $10^{-4.93}$ to $10^{0.37}$ with most QSOs at $R_{\text{edd}} > 0.01$. This is obviously that most QSOs are at $R_{\text{edd}} > 0.01$, while most galaxies cover

the range of $R_{\text{edd}} < 0.01$. As quasars usually have larger luminosity than galaxies, the larger black hole mass will be expected if two populations have similar accretion rate. The slightly larger BH mass in galaxies would be related with the lower accretion rate/Eddington ratio in these sources as shown in Figure 9, although they have lower luminosities than quasars.

4.3 M_{BH} , R_{edd} versus LS

The radio linear size is available for 109 sources from the literature, out of which 89 have BH masses, and 85 sources have Eddington ratio measurements. The distributions between linear size and BH mass, and Eddington ratio are shown in Figure 10. To further study this, we tentatively took 69 low-redshift large-scale radio galaxies in Hu et al. (2016) as a comparison sample. The BH masses and Eddington ratios were directly collected from their work, which were originally used to study the accretion properties. The linear size of these sources were taken from the literature. The comparison in Figure 10 shows that the spread in M_{BH} for our young radio sources is much larger than large-scale radio galaxies. A large fraction of young radio AGNs (77 out of 89, i.e., $\sim 87\%$) have comparable BH masses to large-scale radio galaxies ($> 10^8 M_{\odot}$), however the rest objects have relatively lower black hole masses. The mean values of BH masses are $10^{8.64} M_{\odot}$, and $10^{8.92} M_{\odot}$ for young radio AGNs, and large-scale radio galaxies, respectively. We found a mild correlation at 98% confidence level between LS and BH mass for the combined sample of young radio AGNs and large-scale

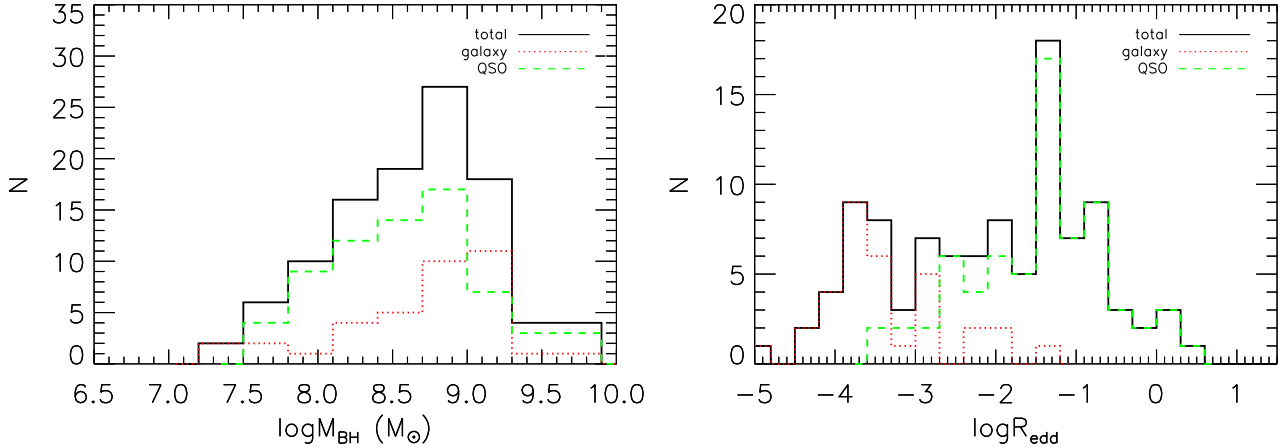


Figure 9. Histogram of the black hole mass (*left*) and Eddington ratio (*right*) of our sample.

radio galaxies. This indicates systematically lower black hole masses in young radio AGNs in comparison to large-scale radio galaxies. In contrast, we only found a trend of decreasing Eddington ratio with increasing LS in the combined sample. The mean values of Eddington ratio are $10^{-2.26}$ and $10^{-3.05}$ for young radio AGNs, and large-scale radio galaxies, respectively.

4.4 NLS1s

According to the criteria to classify a source as NLS1 of $\text{FWHM}(\text{H}\beta)_{\text{broad}} < 2000 \text{ km s}^{-1}$ (Osterbrock & Pogge 1985; Goodrich 1989) or 2200 km s^{-1} (Zhou et al. 2006), $\text{flux}(\text{total } [\text{O III}] \lambda 5007) / \text{flux}(\text{total } \text{H}\beta) < 3$ and $R_{4750} > 0.4$ (Véron-Cetty, Véron & Gonçalves 2001), which is defined as the flux ratio R_{4750} of Fe II complex between rest wavelength 4434 Å and 4684 Å to that of total Hβ, we find one NLS1s in our sample (SDSS J133108.29+303032.9) within 11 sources (1 GPS, 1 HFP and 9 CSS) with measurements of broad Hβ, [O III] line and R_{4750} . Its original spectra and spectral fitting are presented in Figure 11.

SDSS J133108.29+303032.9 ($z = 0.850$, CSS source) has two spectroscopic observations in SDSS. The spectral region around Hβ was analyzed on the BOSS spectrum with a median S/N of 37 and strong Fe II emission. The Hβ can be well modeled with two broad Gaussians and one narrow Gaussian. Each of the [O III] $\lambda\lambda 4959, 5007$ lines was fitted using two Gaussians. The position and width of the core and wing component of [O III] $\lambda 4959$ were separately tied to those of [O III] $\lambda 5007$, and the FWHM of narrow Hβ was tied to that of [O III] $\lambda 5007$ core component. We found that the line width of broad Hβ is $\text{FWHM} = 2073.65 \text{ km s}^{-1}$, and the flux ratio of [O III] $\lambda 5007$ to total Hβ is 1.02. The relative Fe II emission, R_{4750} is 0.88. Following the criterion in Zhou et al. (2006), SDSS J133108.29+303032.9 can be classified as NLS1. Using the line width and luminosity of broad Hβ, the black hole mass can be estimated, $\log M_{\text{BH}} = 8.14 M_{\odot}$, from Equation (2). By combining the luminosity of broad Hβ and Mg II lines, we calculated the BLR luminosity $\log L_{\text{BLR}} = 44.58 \text{ erg s}^{-1}$, and thus the bolometric luminosity $\log L_{\text{bol}} = 45.58 \text{ erg s}^{-1}$ following the method in Section 4.1. The Eddington ratio of the source is 0.20. SDSS J133108.29+303032.9 is very radio loud with a radio

loudness of $\log R = 4.82$, which defined as the ratio between the 5 GHz and 2500 Å rest-frame flux densities.

We plotted the FWHM of $(\text{H}\beta)_{\text{broad}}$ and Fe II strength R_{4750} in Figure 12 to look the position of SDSS J133108.29+303032.9 with other sources (1 GPS, 1 HFP and 8 CSS) in which the broad Hβ and Fe II emission were measured. The plot shows that SDSS J133108.29+303032.9 locates the different space with others, especially performs apparently high Fe II emission. From the Figure 12, we find that HFP and GPS sources locate the same space with non-NLS1s.

4.5 $L_{[\text{O III}]}$ vs. $L_{5\text{GHz}}$

We investigated the relationship between the [O III] $\lambda 5007$ core and the radio (5 GHz) luminosity aiming to study the relationship between optical and radio properties. The relationship between them is shown in Figure 13 for 35 quasars and 33 galaxies where the typical uncertainty on $L_{[\text{O III}]}$ is $< 10\%$ in our spectral measurement, while it is $3\% - 10\%$ for $L_{5\text{GHz}}$ from the literature. We find a significant correlation between $L_{[\text{O III}]}$ and $L_{5\text{GHz}}$ with a Spearman rank correlation coefficient $r_s = 0.72$, and a probability P_{null} less than 10^{-10} for the null hypothesis of no correlation. It is evident that quasars tend to be brighter in both luminosities than galaxies, which may be caused by the fact that many of quasars are at higher redshift than galaxies (see Figure 13). We employed the partial Kendall's τ correlation test (Akritas & Siebert 1996) to assess the correlation between $L_{5\text{GHz}}$ and $L_{[\text{O III}]}$ eliminating the effect of redshift. Our partial test shows that the strong positive correlation still present with partial correlation coefficients $\tau = 0.2$ and $P_{\text{null}} = 0.0047$. The Ordinary Least Squares bisector (OLS bisector) method (Isobe, Feigelson, Akritas & Babu 1990) fit to the correlation between $L_{[\text{O III}]}$ and $L_{5\text{GHz}}$ is $\log L_{5\text{GHz}} = 1.38(\pm 0.09) \times \log L_{[\text{O III}]} - 22.18(\pm 2.98)$.

The strong correlation between $L_{[\text{O III}]}$ of core [O III] $\lambda 5007$ and $L_{5\text{GHz}}$ for 68 objects in our sample suggests that jet activity is strongly associated with accretion process in young radio AGNs as the luminosity of core [O III] $\lambda 5007$ can trace nuclei radiation (Son et al. 2012). However, the dependence of $L_{5\text{GHz}}$ on $L_{[\text{O III}]}$ is steeper than that of Xu et al. (1999) for a sample of radio-loud AGNs with available data

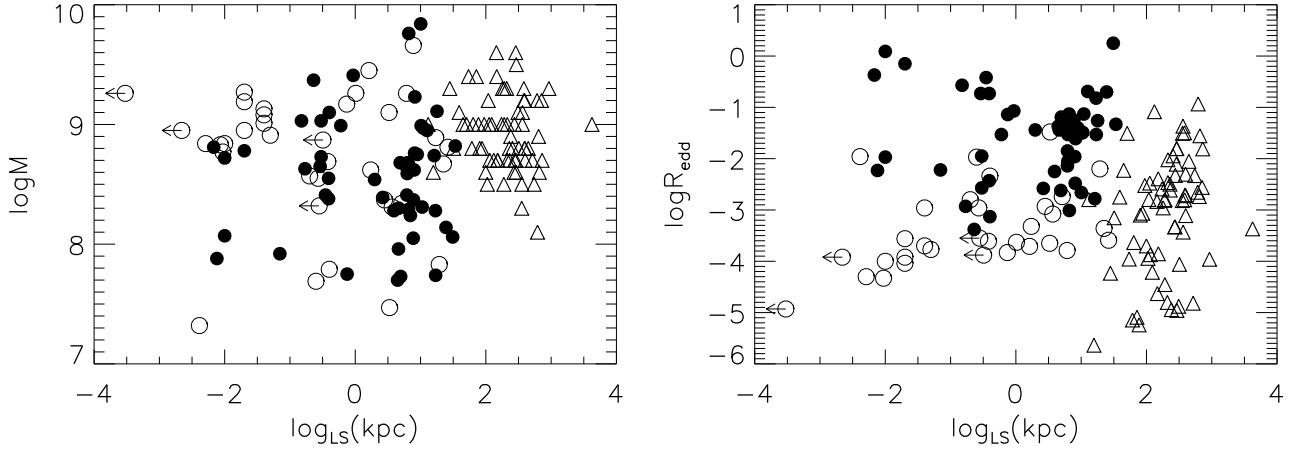


Figure 10. BH mass versus linear size (*left*) and Eddington ratio vs. linear size (*right*). The filled and open circles are young radio AGNs in our sample classified as quasar and galaxy, respectively. The triangles are large-scale radio galaxies in Hu et al. (2016), used as comparison. The arrows represent the upper limits on the linear size.

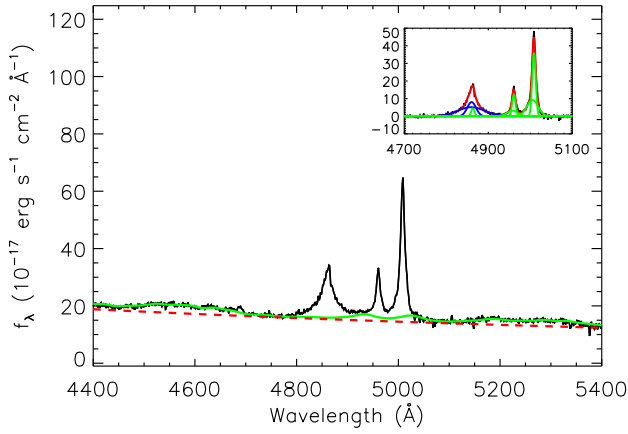


Figure 11. The spectral fitting for two sources classified as NLS1s: SDSS J133108.29+303032.9 Lines as in Figure 3.

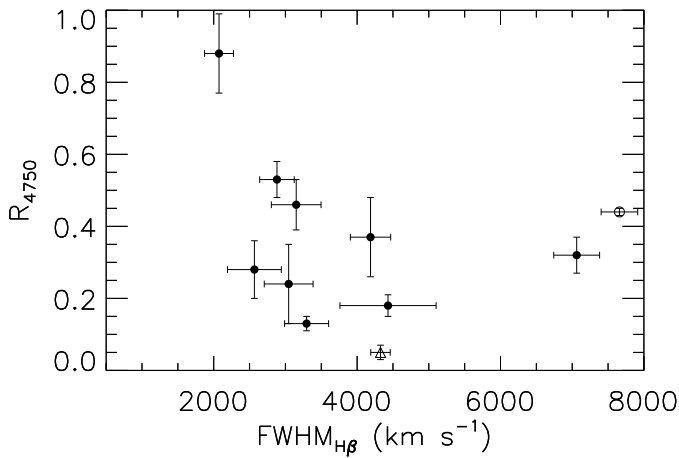


Figure 12. Fe II strength against the FWHM of $(H\beta)_{\text{broad}}$. The filled circles, the open circle and the open triangle represent CSS, GPS and HFP sources, respectively.

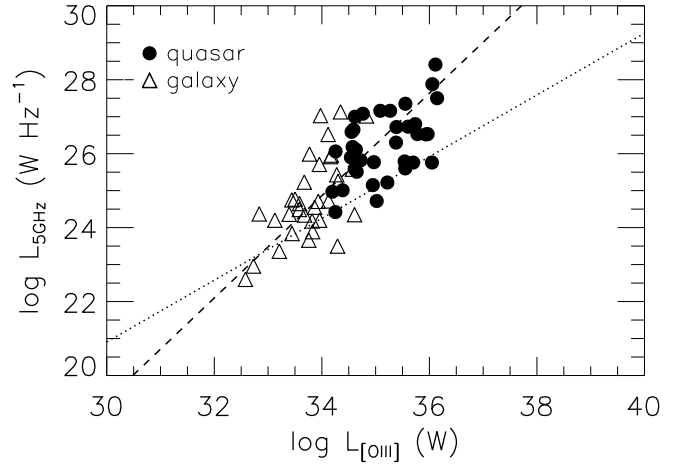


Figure 13. The radio luminosity $L_{5\text{GHz}}$ versus the luminosity of $[OIII]\lambda 5007$ line core. The filled circles and open triangles stand for quasars and galaxies, respectively. The dashed line is the OLS bisector fit for our sources, while the dotted line denotes the relation of normal radio-loud AGNs derived from OLS bisector fit in Xu et al. (1999).

collected from the literature at that time. Their relation is indicated in Figure 13 as a dotted line derived from the same method of OLS bisector. We find that most of our sources lie above their relation, indicating that young radio AGNs have stronger radio emission than that of normal radio-loud AGNs at given $L_{[OIII]}$. This supports the evolution scenario where young, compact AGNs are more efficient radio emitters than normal, large-scale objects, and will eventually evolve into the latter population.

4.6 The optical variability of quasars

We studied the optical variability of quasars based on SDSS multi-epoch spectroscopy. To study the variability of continuum emission, we selected those quasars with $D_{4000} \leq 1$ to minimize the contribution of host galaxy, and we fitted the continuum on global spectra. There are in total 15 quasars (i.e., 8 CSS, 5 HFP, 1 GPS and 1 CSO) with multiple spec-

troscopic observations, of which 12 were observed twice, 3 more than two times. The source list and the measurements of continuum and emission lines are given in Table 3. The redshift of these sources range from 0.230 to 3.593, with most objects at $z > 0.8$ (see Table 3).

We used the integrated flux of overall spectrum where the wavelength range (in the rest-frame) correspond to the overlaps of SDSS and BOSS spectra from 3800 to 9200 Å at observed frame to study the source variability. The source variability was determined by comparing the variation between the brightest and faintest spectra as $\Delta f = (f_{\text{int,b}} - f_{\text{int,f}})/f_{\text{int,f}}$, where $f_{\text{int,b}}$ and $f_{\text{int,f}}$ are integrated flux at the brightest and faintest epochs, respectively) (e.g., Guo & Gu 2016). We also corrected the systematic difference between BOSS and SDSS DR7 spectra by dividing the BOSS spectrum by the systematic correction spectrum of Guo & Gu (2016) before spectra fitting when BOSS spectrum is involved.

The distribution of the optical variabilities Δf of 15 objects is shown in Figure 14. All CSS/GPS/HFP/CSO sources distribute at low variability $\leq 60\%$.

The color variation for every object was evaluated from the difference in the spectral index between the bright and faint epochs, $\Delta\alpha = \alpha_b - \alpha_f$, where α_b and α_f are the spectral indices at brightest and faintest epochs, respectively. It was further checked by the power-law fit on the difference spectrum between two epochs (see details in Guo & Gu 2016). Considering $\sim 4\%$ spectrophotometry uncertainty in SDSS spectra (Adelman-McCarthy et al. 2008), we conservatively studied the color variation only in 7 out of 15 sources, which have reliable variations $\Delta f > 20\%$. The consistent color variations between the spectral index difference and the power-law fit on the difference spectrum are found in 6 out of these 7 sources, which all exhibit bluer-when-brighter (BWB) trend (see Table 3).

We failed to find any significant variations in the line width of broad H β , Mg II and C IV lines for all sources studied. The luminosities of broad emission lines also do not change significantly in all sources, except for SDSS J104406.33+295900.9, of which C IV emission at bright epoch is larger than the faint one by about a factor of 2.5 at $> 3\sigma$ significance (see Table 3).

Guo & Gu (2016) investigated the optical variability for a sample of 2169 quasars with a large redshift coverage, in which most sources are radio-quiet. Their results showed that the variability of most objects is below 60%. In our sample, we find that all CSS/GPS/HFP/CSO sources have variability below 60%, similar to radio-quiet quasars of Guo & Gu (2016), implying that the variability mechanism in these sources could be similar to radio-quiet quasars and the jet does not contribute much in variability mainly due to large jet viewing angle.

5 DISCUSSIONS

In this work, we investigated the optical properties for a sample of young radio AGNs constructed from SDSS DR12, which includes GPS, CSS, HFP and CSO radio sources.

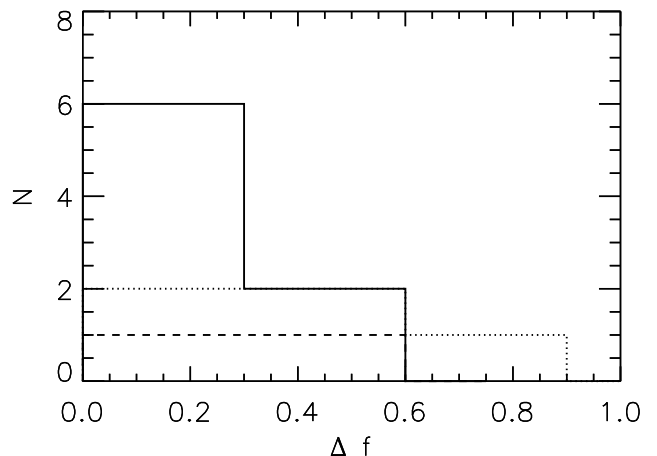


Figure 14. Distribution of the optical variabilities of 15 quasars with multi-epoch SDSS spectroscopy. CSS sources are shown as solid line, HFP sources as dotted line and the dashed line is for GPS/CSO sources.

5.1 Black hole mass and accretion mode

While the empirical relation between the radius of broad line region and continuum luminosity was commonly used to estimate the black hole mass in large sample of AGNs (e.g., Shen et al. 2011), its applicability was evaluated and then the continuum luminosity was replaced by BLR luminosity for radio-loud AGNs to avoid the overestimation of the black hole mass due to the jet contribution on the continuum emission (e.g., Kong et al. 2006). Previous studies have shown that at least some GPS and extreme GPS (i.e., HFP) sources may present beaming effect (O’Dea 1998), which could be less significant in CSS sources due to large jet viewing angles. As shown in Section 4.2.1, the deviation from radio-quiet AGNs strongly favor the presence of jet emission. It thus is more reasonable to calculate black hole mass by using BLR luminosity. The black hole masses estimated in this way in our sample cover a broad range, consistent with Wu (2009) and Son et al. (2012).

Compared to M_{BH} distribution, the Eddington ratios cover even a broader range from $10^{-4.93}$ to $10^{0.37}$, suggesting diversities of accretion activities as found in Son et al. (2012). Particularly, quasars tend to have higher Eddington ratios than galaxies in our sample, mostly at > 0.01 . Adopting a rough dividing value of Eddington ratio, 0.01, between the optically thin advection-dominated accretion flow and optically thick standard accretion disc (Narayan & Yi 1995), there exists two accretion modes in our sample.

We find that the Eddington ratios of about 46% of the sources are below 0.01, of which most are narrow-line objects. Most of the low radio luminosity sources ($L_{5\text{GHz}} < 10^{26} \text{ W Hz}^{-1}$) (Snellen et al. 2004; Kunert-Bajraszewska et al. 2010; Stanghellini et al. 2009) locate at the range of $R_{\text{edd}} < 0.01$ (see Figure 15). In the study of Kunert-Bajraszewska et al. (2010), it showed that low-luminosity CSS radio sources can be classified as HEGs and LEGs, where they are usually associated with accreting in a radiatively efficient manner at high Eddington ratio ($R_{\text{edd}} > 0.01$) and exhibiting radiatively inefficient accretion related to low Eddington ratio ($R_{\text{edd}} < 0.01$), respec-

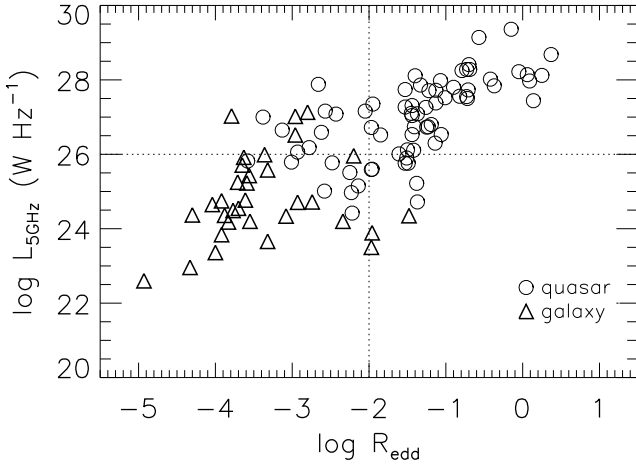


Figure 15. The radio luminosity $L_{5\text{GHz}}$ versus the Eddington ratio R_{edd} . The circles and triangles stands for QSOs and galaxies, respectively. The vertical and horizontal dotted lines are indicated as the separations of high and low luminosity (10^{26}), and high and low Eddington ratio (0.01), respectively.

tively (Padovani et al. 2017). Thus, our sources with low luminosity and low Eddington ratio below 0.01 may be the LEGs counterparts. We summarized the information of radio classification (CSS/GPS/HFP/CSO) and optical type (type1/type2 and HEG/LEG) in Table 4 with the estimated Eddington ratio, in which the HEGs and LEGs classification were based on EI value larger and smaller than 0.95 estimated using equation (7) from Buttiglione et al. (2010) for the sources of which the measures were possible for related lines, respectively. We find that for the classified HEG and LEG sources, most of them separately correspond the $R_{\text{edd}} > 0.01$ and $\log R_{\text{edd}} < 0.01$.

$$\text{EI} = \log \frac{[\text{O III}]}{\text{H}\beta} - \frac{1}{3} \left(\log \frac{[\text{N II}]}{\text{H}\alpha} + \log \frac{[\text{S II}]}{\text{H}\alpha} + \log \frac{[\text{O I}]}{\text{H}\alpha} \right) \quad (7)$$

The strong positive correlation between the Eddington ratio and the radio luminosity at 5 GHz in our sample shown in Figure 15, implies that the accretion process is correlated with radio emission in young radio AGNs with stronger radio emission when higher accretion ratio.

The mixed accretion modes as shown in young radio AGNs have implication that young jet activity could happen in various accretion systems, in others words, the sources at early stage of jet evolution are not necessarily only associated with the system with high accretion rate.

5.2 Evolution

The evolution of radio sources generally can be studied either using radio luminosity vs LS as done in An & Baan (2012) and Kunert-Bajraszewska et al. (2010), or using $L_{[\text{OIII}]}$ versus LS (Kunert-Bajraszewska & Labiano 2010). The long-term evolutionary scenarios were proposed as the smallest radio sources CSO/GPS/HFP (LS < 1kpc) evolve into medium-sized objects CSS (LS < 20 kpc) and eventually evolve into large-scale FR II and FRI sources (LS: tens to several thousand kpc) for high luminosity and low luminosity

radio sources in An & Baan (2012), respectively. While from the optical perspective, Kunert-Bajraszewska & Labiano (2010) suggested that HEGs and LEGs are usually associated with high accretion rate and low accretion rate, respectively, and they follow different evolution. While HEGs objects will follow evolutionary track of $\text{GPS}_{\text{HEG}} - \text{CSS}_{\text{HEG}} - \text{FR}_{\text{HEG}}$, the smallest-scale LEGs sources will evolve to CSS LEG radio sources, finally evolve to large-scale FR LEGs.

In our work, the evolution of young radio AGNs is studied by incorporating the Eddington ratio into the radio power - linear size panel shown in Figure 16. From the radio perspective, our sources generally follow the expected evolutionary tracks towards large-scale sources as the smallest high (low) luminosity CSO/GPS/HFP objects to medium-sized high (low) luminosity CSSs to large-scale high (low) luminosity FR II/FRI sources (An & Baan 2012), where the evolutionary tracks are based on parametric modeling for high luminosity and low luminosity objects, respectively. In addition to the evolution manifested from LS - $L_{5\text{GHz}}$ relation, there is an evident trend of Eddington ratio decreasing with increasing LS for high luminosity radio sources ($L_{5\text{GHz}} > 10^{26} \text{ W/Hz}$), in which median ($\log R_{\text{edd}}$) is -1.44 and -2.52 for high luminosity radio young sources and large-scale FR II radio galaxies, respectively. Similarly, this trend is also seen in low luminosity radio sources with the median ($\log R_{\text{edd}}$) for low luminosity radio young sources and large-scale FRI radio galaxies of -3.01 and -4.23, respectively. These results strongly indicate that the young radio AGNs will eventually evolve into large-scale radio sources in general.

5.2.1 Sources with low luminosity and low accretion rate

The Eddington ratio of low luminosity radio sources in our sample is almost less than 0.01 (see Figure 15). Although the Eddington ratios of these sources overlap with large-scale objects, they are indeed systematically larger than large-scale ones. Therefore, these low-luminosity radio sources with low R_{edd} could still be the ancestors of low-luminosity large-scale FR I sources (see Figure 16). Alternatively, the growing number of observations show that short-lived/dying radio sources may be associated with low-luminosity young radio AGNs (Kunert-Bajraszewska et al. 2010; An & Baan 2012). Their accretion phase(s) last shorter than $10^4 - 10^5$ years and will not evolve into large-scale object which is probably caused by the low accretion rate (Wołoska et al. 2017). This will probably result in compact radio morphology with weak radio emission or faders which show disrupted lobes without hotspots (e.g., breaking-up structures shown in Kunert-Bajraszewska et al. (2010)).

The radio morphology of sources with low luminosity and low accretion rate will be useful to study the source evolution, i.e., well-confined lobes and hotspots structure, or faders, or relics. We try to check the radio morphology for our objects with low luminosity and low Eddington ratio from the previous work (i.e., de Vries et al. 2009; Kunert-Bajraszewska et al. 2010). However we didn't find significant evidence of radio relics (e.g., diffused emission without radio core), thus all these sources are less likely at inactive phase. The the obvious morphology with fading was found in SDSS J155927.67+533054.4 ($\log R_{\text{edd}} = -2.74$, LS = 5.13 pc, $\log L_{5\text{GHz}} = 24.72 \text{ W Hz}^{-1}$) from the 1.5 GHz MERLIN observation showing breaking up struc-

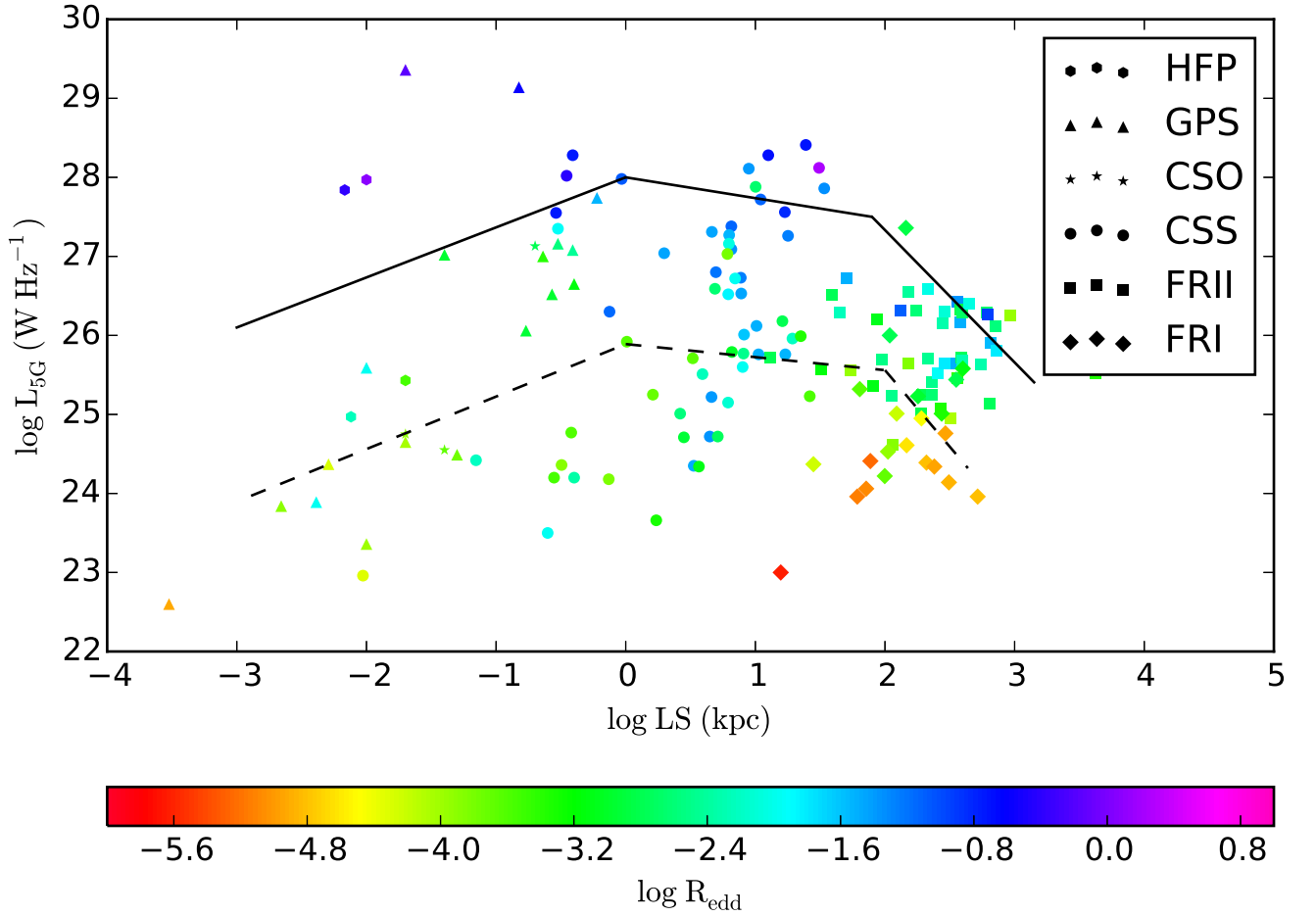


Figure 16. Radio power at 5 GHz vs. linear size with Eddington ratio. The HFP, GPS, CSO, CSS sources are shown as hexagons, triangles, and asterisks and circles, respectively. The squares and diamonds are for FR II and FR I sources, respectively. The value of Eddington ratio is shown with the color bar at bottom. The black solid and dashed lines are the expected evolutionary tracks based on parametric modeling for the high-luminosity and low-luminosity radio sources in An & Baan (2012).

ture with a weak radio core in Kunert-Bajraszewska et al. (2010). The low luminosity sources in our sample SDSS J084856.57+013647.8, SDSS J100955.51+140154.2, SDSS J154349.50+385601.3 and SDSS J154525.48+462244.3 may be also faders and undergo disturbed evolution since they show brightness and polarization asymmetry associated with interaction with surrounding medium in the radio observation in Kunert-Bajraszewska et al. (2010). In SDSS J083139.79+460800.8 ($\log R_{\text{edd}} = -4.04$, $LS = 21$ pc, $\log L_{5\text{GHz}} = 24.65$ W Hz $^{-1}$), a compact double structure is clearly seen from VLBI observation in de Vries et al. (2009). The dynamical age determined by VLBI observations is about 245 ± 55 years in de Vries et al. (2010) and indicates that it is indeed young and may persistently grow up. The similar case is in SDSS J151141.26+051809.2 ($\log R_{\text{edd}} = -2.23$, $LS = 7.6$ pc, $\log L_{5\text{GHz}} = 24.97$ W Hz $^{-1}$) in which the high-resolution VLBI images at 8.4 and 15.4 GHz re-

veal it owns well confined double structure with a radio core in An et al. (2012). The kinematic age based on the proper motion of lobes is 300 ± 140 years (An et al. 2012). Interestingly, SDSS J124733.31+672316.4 ($\log R_{\text{edd}} = -3.92$, $LS = 145$ pc, $\log L_{5\text{GHz}} = 24.75$ W Hz $^{-1}$) shows double-double morphology based on VLBI observations (Marecki et al. 2003), suggesting restarted accretion and radio activities (An & Baan 2012). Moreover, several sources (e.g., J093609.36+331308.3, J105731.17+405646.1, J140051.58+521606.5 and J143521.67+505122.9) are unresolved in VLBI images (de Vries et al. 2009). As shown in Wołowska et al. (2017), these sources may be the transient radio sources (associate with short-lived radio sources) in temporary low accretion state with weak radio emission and compact morphology. Higher resolution radio observations will be needed to unveil their detailed morphology, especially for SDSS J105731.17+405646.1, the source with the

lowest Eddington ratio in our sample ($\log R_{\text{edd}} = -4.93$). In summary, the young radio sources with low luminosity and low accretion rate show various radio properties and activities, including short-lived/dying/transient sources, restarted sources and normal evolved sources.

5.2.2 Implication from M_{BH} and R_{edd}

Naively expected, the sources with smaller LS may generally have lower BH mass and higher accretion rate. Therefore, the BH mass (accretion rate) is expected to positively (negatively) correlate with the LS in young radio AGNs. However these two trends are not evident in our sample sources alone (see Figure 10), perhaps due to the intrinsic diversities of accretion in young radio AGNs.

The diversity in BH and Eddington ratio is further supported by our results in Figure 17 with the distribution of black hole masses along with the Eddington ratios, where young radio AGNs in our sample can be divided into three parts using the dividing values of black hole mass $10^8 M_{\odot}$ and Eddington ratio 0.01. Our sources in part three occupy the region of lower black hole masses and higher Eddington ratios compared to large-scale objects. They are similar to NLS1s, thus could be candidates of both accretion and jet at early evolutionary stage. However, some young radio AGNs overlapping with large-scale sources are also found (parts one and two in Figure 17). The sources in part one have comparable black hole masses and Eddington ratios with large-scale radio galaxies, corresponding to the sources with low radio luminosity and Eddington ratio mentioned in Section 5.2.1. Some of them may be restarted sources since they already have comparable black hole masses with large-scale objects. This is strongly supported by the double-double morphology as shown in SDSS J124733.31+672316.4 ($\log M_{\text{BH}} = 8.95$, also see Section 5.2.1). The second box in Figure 17 consists of objects with similar black hole masses however higher Eddington ratios than large-scale ones. They may also be restarted sources however at higher accretion state than part one objects. Interestingly, there are few sources at the lower-left corner in Figure 17. This is probably because these sources are very weak, thus missed in various surveys.

5.3 NLS1s & young radio AGNs

Several studies have focused on the association between young radio AGNs and NLS1s (Yuan et al. 2008; Caccianiga et al. 2014; Gu et al. 2015; Berton et al. 2015; Caccianiga et al. 2017). Some of these two populations show similar radio morphology (Gu et al. 2015; Caccianiga et al. 2017) and are in the same range of black hole masses and Eddington accretion rates (Wu 2009; Berton et al. 2016). The hypothesis of CSS-like sources as the parent population of flat-spectrum RLNLS1s has been proposed by Berton et al. (2015). Within 11 sources (1 GPS, 1 HFP and 9 CSS) with measurements of broad $H\beta$ and $[O III]$, we find one NLS1s (CSS source: SDSS J133108.29+303032.9), i.e., about 11% detection rate in CSS sources. In contrast, there are seven CSS-like sources in 14 RLNLS1s of Gu et al. (2015), and six CSS-like sources out of 19 RLNLS1s in Gu et al. (2019, in preparations), resulting in a fraction of $\sim 39\%$ CSS-like sources in RLNLS1s. The discrepancy of source fraction indicates that a high fraction (39%) of radio-loud NLS1s are

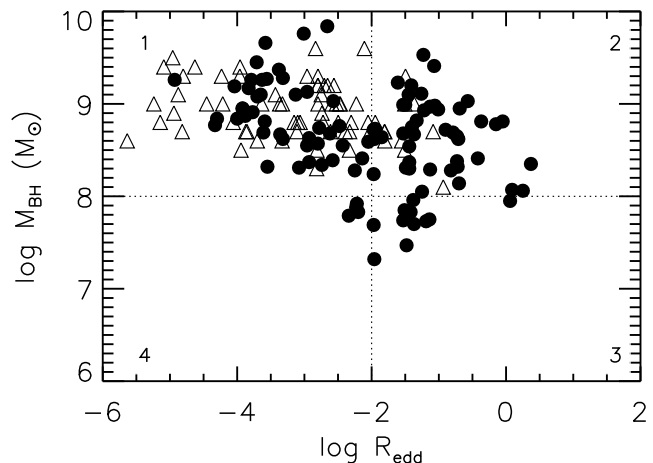


Figure 17. The BH mass vs. Eddington ratio for our young radio AGNs donated by filled circles and large-scale FR I/FR II radio galaxies of Hu et al. (2016) shown as triangles.

CSS sources but that only 11% of CSS are RL NLS1s. It is likely due to the observational biases, i.e., the missed large-scale extended radio emission in previous studies, as demonstrated in Richards & Lister (2015) that such extended emission may be common, at least among the brightest radio-loud NLS1s, based on the high-sensitivity JVLA observations.

Interestingly, the one NLS1 in our sample differ from others in many aspects, especially in γ -ray emission. SDSS J133108.29+303032.9, well known as 3C 286, has a core-jet structure on pc-scale with an inclination angle of 48° between the line of sight and jet (An et al. 2017). It has been identified in the third Fermi-LAT source catalogue (Acero et al. 2015). However, the origin of γ -ray emission is unclear, which may be due to the interaction between jet and interstellar medium (ISM) (Migliori et al. 2014). The BOSS spectrum shows obvious blueshifted $[O III]$ wing, which may be induced by outflow or jet-ISM interaction (Gelderman & Whittle 1994; Kim et al. 2013). The obtained broad $H\beta$ line width of the source is consistent with Berton et al. (2017) within error.

5.4 Selection effect

It should be noticed that our collection of young radio sources (starting samples) cannot be certainly considered as statistically complete and representative of the entire population due to the radio-selected samples we used have been selected using different techniques (e.g., spectral shape and peak frequency, and/or radio morphology). While it is difficult to evaluate the completeness of parent sample, we tried to study the representative of final optical sample in respect to parent sample as we requested SDSS spectrum. The distributions of radio luminosity at 5 GHz and redshift are compared in two samples (see Figure 18). The median values of redshift in optical and parent samples are 0.452 and 0.656, respectively, implying the redshift is systematically lower in optical sample. For $L_{5\text{GHz}}$, the optical sample is systematically less than parent sample, with the median values of 26.11 and 27.00 W Hz^{-1} , respectively. The K-S test results show that $L_{5\text{GHz}}$ and redshift distribution of two samples are

indeed different. It seems that our optical sample is biased towards low-redshift and low-luminosity compared with parent sample.

As shown in Figure 18, the source fraction of our optical sample to parent sample is less than 40% at $L_{5\text{GHz}} < 23.7 \text{ W Hz}^{-1}$ and $L_{5\text{GHz}} > 26.1 \text{ W Hz}^{-1}$, implying under-representative in these luminosity ranges. We evaluated the effect of the missed sources in the two luminosity ranges by estimating the bolometric luminosity from available R magnitude in the automated Million Optical Radio/X-ray Associations (MORX) catalog (Flesch 2016), assuming $L_{\text{bol}} = 9.26 \lambda L_{5100}$ (Shen et al. 2011), in which luminosity at 5100 \AA L_{5100} was calculated from R magnitude assuming a spectral index of 0.5. The possible location of each missed sources is shown as a dotted line in Figure 19 because the black hole mass is unknown. Although two targets is a bit far from our sample sources of which they are possibly detected in part 4 depending on black hole mass, We found that most missed sources have Eddington ratio larger than 10^{-3} at the black hole mass range covered by our sample sources. Therefore, the missed sources will not affect our results significantly in Figure 16.

6 CONCLUSIONS

We built a largest sample of 126 young radio AGNs with spectroscopy from SDSS DR12 up to now in order to study their accretion, evolution and search NLS1s candidates. Stellar velocity dispersion versus gas velocity dispersion, jet-disk relation and optical variability are also investigated.

We find that the black hole masses and Eddington ratios cover a wide range, suggesting that our sources have different levels of accretion activity and not all of young radio AGNs are accreting at high accretion rate. In the distribution of the radio power and linear size, we find that high and low luminosity radio sources separately follow the global evolutionary trend with increasing linear size and decreasing accretion rate towards large-scale radio sources. We also discussed the radio properties of sources with low Eddington ratio and low radio luminosity. By comparing the stellar velocity dispersion and line width of [O III], we find that the line width of core of [O III] $\lambda 5007$ can be used as a good surrogate of stellar velocity dispersion. The radio power correlates strongly with [O III] $\lambda 5007$ core luminosity in our work, suggesting that radio activities and accretion are closely related. We also find one object can be defined as narrow-line Seyfert 1 galaxies (NLS1s), representing a population of young AGNs both with young jets and early accretion activities. The optical variabilities of 15 quasars with multi-epoch spectroscopy were investigated. Our results show that the optical variability in young AGN quasars is similar to radio-quiet quasars, supporting the previous results (O’Dea 1998) that no significant variability in general for young radio AGNs.

ACKNOWLEDGEMENTS

We thank the anonymous referee for comments and suggestions to improve the manuscript. We thank Ting Xiao for help with spectral analysis. This work is supported by the National Science Foundation of China (grants 11873073,

U1531245, 11773056, and 11473054, U1831138). Funding for SDSS-III has been provided by the Alfred P. Sloan Foundation, the Participating Institutions, the National Science Foundation, and the U.S. Department of Energy Office of Science. The SDSS-III web site is <http://www.sdss3.org/>. This research has made use of the NASA/IPAC Extragalactic Database (NED) which is operated by the Jet Propulsion Laboratory, California Institute of Technology, under contract with the National Aeronautics and Space Administration. We acknowledge the support of the staff of the Lijiang 2.4m telescope. Funding for the telescope has been provided by CAS and the People’s Government of Yunnan Province.

REFERENCES

- Acero, F., Ackermann, M., Ajello, M., et al. 2015, *ApJS*, 218, 23
Adelman-McCarthy, J. K., Agüeros, M. A., Allam, S. S., et al. 2008, *ApJS*, 175, 297
Akritas M. G., Siebert J., 1996, *MNRAS*, 278, 919
An, T., & Baan, W. A. 2012, *ApJ*, 760, 77
An, T., Wu, F., Yang, J., et al. 2012, *ApJS*, 198, 5
An, T., Lao, B.-Q., Zhao, W., et al. 2017, *MNRAS*, 466, 952
Bachev, R., Marziani, P., Sulentic, J. W., et al. 2004, *ApJ*, 617, 171
Bai, J. M., & Liu, Z. 2010, *Gaia Follow-up Network for Solar System Objects*, 63
Baker, J. C., & Hunstead, R. W. 1995, *ApJ*, 452, L95
Balogh, M. L., Morris, S. L., Yee, H. K. C., Carlberg, R. G., & Ellingson, E. 1999, *ApJ*, 527, 54
Becker, R. H., White, R. L., & Edwards, A. L. 1991, *ApJS*, 75, 1
Berton, M., Caccianiga, A., Foschini, L., et al. 2016, *A&A*, 591, A98
Berton, M., Foschini, L., Caccianiga, A., et al. 2017, *Frontiers in Astronomy and Space Sciences*, 4, 8
Berton, M., Foschini, L., Ciroi, S., et al. 2015, *A&A*, 578, A28
Best, P. N., & Heckman, T. M. 2012, *MNRAS*, 421, 1569
Best P. N., Kauffmann G., Heckman T. M., Ivezić Ž., 2005, *MNRAS*, 362, 9
Bolton, R. C., Cotter, G., Pooley, G. G., et al. 2004, *MNRAS*, 354, 485
Boroson T. A. 2003, *ApJ*, 585, 647
Buttiglione, S., Capetti, A., Celotti, A., et al. 2010, *A&A*, 509, A6
Caccianiga, A., Antón, S., Ballo, L., et al. 2014, *MNRAS*, 441, 172
Caccianiga, A., Dallacasa, D., Antón, S., et al. 2017, *MNRAS*, 464, 1474
Cao, X., & Jiang, D. R. 1999, *MNRAS*, 307, 802
Cao, X., & Jiang, D. R. 2001, *MNRAS*, 320, 347
Cappellari, M. 2017, *MNRAS*, 466, 798
Cappellari, M., & Emsellem, E. 2004, *PASP*, 116, 138
Celotti, A., Padovani, P., & Ghisellini, G. 1997, *MNRAS*, 286, 415
Chandola, Y., Sirothia, S. K., & Saikia, D. J. 2011, *MNRAS*, 418, 1787
Cracco, V., Ciroi, S., Berton, M., et al. 2016, *MNRAS*, 462, 1256
Cui, L., Liu, X., Liu, J., Song, H.-G., & Ding, Z. 2010, *A&A*, 518, A23
Dallacasa, D., Stanghellini, C., Centonza, M., & Fanti, R. 2000, *A&A*, 363, 887
D’Ammando, F., Orienti, M., Finke, J., et al. 2013, *MNRAS*, 436, 191
de Vries, N., Snellen, I. A. G., Schilizzi, R. T., Mack, K.-H., & Kaiser, C. R. 2009, *A&A*, 498, 641

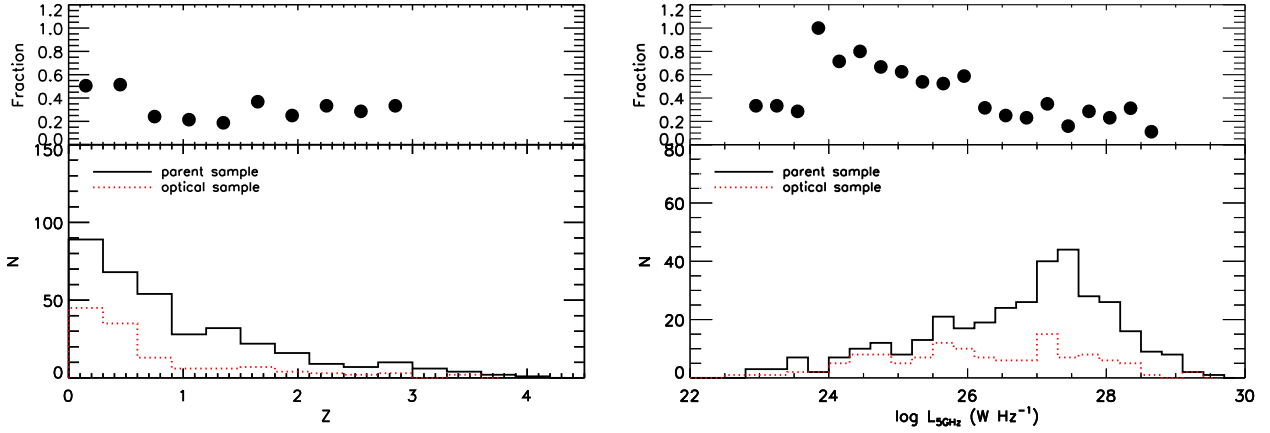


Figure 18. Redshift distribution (*left*) and $L_{5\text{GHz}}$ distribution (*right*) between parent and optical sample. The upper plots are the source fraction for redshift and $L_{5\text{GHz}}$ of optical sample to parent sample, respectively. The red dotted line and black solid line stands for optical sample and parent sample, respectively.

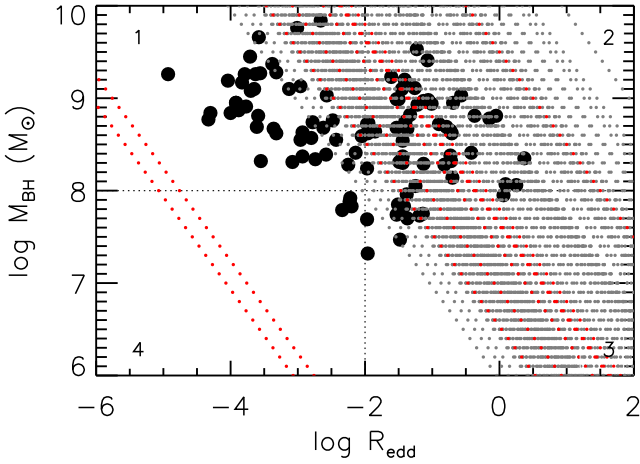


Figure 19. The BH mass vs. Eddington ratio for young radio AGNs donated by filled circles and missed sources shown as dotted lines in which the grey ones and the red ones represent the possible location for the missed high luminosity sources with $L_{5\text{GHz}} > 26.1 \text{ W Hz}^{-1}$ and the missed low luminosity sources with $L_{5\text{GHz}} < 23.7 \text{ W Hz}^{-1}$, respectively.

de Vries, N., Snellen, I. A. G., Schilizzi, R. T., & Mack, K.-H. 2010, *A&A*, 521, A2
Dong, X.-B., Zhou, H.-Y., Wang, T.-G., et al. 2005, *ApJ*, 620, 629
Edwards, P. G., & Tingay, S. J. 2004, *A&A*, 424, 91
Fanti, C., Pozzi, F., Dallacasa, D., et al. 2001, *A&A*, 369, 380
Fanti, R., Fanti, C., Schilizzi, R. T., et al. 1990, *A&A*, 231, 333
Farina, E. P., Decarli, R., Falomo, R., Treves, A., & Raiteri, C. M. 2012, *MNRAS*, 424, 393
Ferrarese, L., & Merritt, D. 2000, *ApJ*, 539, L9
Flesch, E. W. 2016, *Publ. Astron. Soc. Australia*, 33, e052
Francis, P. J., Hewett, P. C., Foltz, C. B., et al. 1991, *ApJ*, 373, 465
Gelderman, R., & Whittle, M. 1994, *ApJS*, 91, 491
Giroletti, M., & Polatidis, A. 2009, *Astronomische Nachrichten*, 330, 193
Goodrich, R. W. 1989, *ApJ*, 342, 224
Greene, J. E., & Ho, L. C. 2005, *ApJ*, 627, 721
Greene, J. E., & Ho, L. C. 2005, *ApJ*, 630, 122
Guo, H., & Gu, M. 2016, *ApJ*, 822, 26

Gu, M., & Ai, Y. L. 2011, *A&A*, 528, A95
Gu, M., Cao, X., & Jiang, D. R. 2009, *MNRAS*, 396, 984
Gu, M., & Chen, Y. 2010, *AJ*, 139, 2612
Gu, M., Chen, Y., Komossa, S., et al. 2015, *ApJS*, 221, 3
Heckman, T. M., Kauffmann, G., Brinchmann, J., et al. 2004, *ApJ*, 613, 109
Helmholtz, J. F., Taylor, G. B., Tremblay, S., et al. 2007, *ApJ*, 658, 203
Holt, J., Tadhunter, C. N., & Morganti, R. 2008, *MNRAS*, 387, 639
Horiuchi, S., Fomalont, E. B., Taylor, W. K., et al. 2004, *ApJ*, 616, 110
Hu, J.-F., Cao, X.-W., Chen, L., & You, B. 2016, *Research in Astronomy and Astrophysics*, 16, 136
Isobe T., Feigelson E. D., Akritas M. G., Babu G. J., 1990, *ApJ*, 364, 104
Kim, M., Ho, L. C., Lonsdale, C. J., et al. 2013, *ApJ*, 768, L9
Komossa S., 2008, *RMxAC*, 86, *RMxAC*.32
Komossa, S., Voges, W., Xu, D., et al. 2006, *AJ*, 132, 531
Komossa, S., & Xu, D. 2007, *ApJ*, 667, L33
Kong, M.-Z., Wu, X.-B., Wang, R., & Han, J.-L. 2006, *Chinese J. Astron. Astrophys.*, 6, 396
Kormendy, J., & Ho, L. C. 2013, *ARA&A*, 51, 511
Kunert-Bajraszewska, M., Gawroński, M. P., Labiano, A., & Siemiginowska, A. 2010, *MNRAS*, 408, 2261
Kunert-Bajraszewska, M., & Labiano, A. 2010, *MNRAS*, 408, 2279
Kunert, M., Marecki, A., Spencer, R. E., Kus, A. J., & Niezgoda, J. 2002, *A&A*, 391, 47
Labiano, A. 2008, *A&A*, 488, L59
Labiano, A., Barthel, P. D., O'Dea, C. P., et al. 2007, *A&A*, 463, 97
Laurent-Muehleisen, S. A., Kollgaard, R. I., Ryan, P. J., et al. 1997, *A&AS*, 122, 235
Lister, M. L., Aller, M. F., Aller, H. D., et al. 2016, *AJ*, 152, 12
Liu, Y., Jiang, D. R., & Gu, M. F. 2006, *ApJ*, 637, 669
Marecki, A., Barthel, P. D., Polatidis, A., & Owsianik, I. 2003, *Publ. Astron. Soc. Australia*, 20, 16
Massaro, E., Giommi, P., Leto, C., et al. 2009, *A&A*, 495, 691
McConnell, N. J., & Ma, C.-P. 2013, *ApJ*, 764, 184
Migliori, G., Siemiginowska, A., Kelly, B. C., et al. 2014, *ApJ*, 780, 165
Mingaliev, M. G., Sotnikova, Y. V., Tornainen, I., Tornikoski, M., & Udovitskiy, R. Y. 2012, *A&A*, 544, A25
Murgia, M. 2003, *Publ. Astron. Soc. Australia*, 20, 19
Narayan, R., & Yi, I. 1995, *ApJ*, 452, 710

- Nelson, C. H., & Whittle, M. 1996, *ApJ*, 465, 96
- O’Dea, C. P. 1998, *PASP*, 110, 493
- O’Dea, C. P., de Vries, W. H., Koekemoer, A. M., et al. 2002, *AJ*, 123, 2333
- Orienti, M., & Dallacasa, D. 2008, *A&A*, 479, 409
- Orienti, M., & Dallacasa, D. 2012, *MNRAS*, 424, 532
- Orienti, M., Dallacasa, D., & Stanghellini, C. 2007, *A&A*, 475, 813
- Orienti, M., Dallacasa, D., & Stanghellini, C. 2010, *MNRAS*, 408, 1075
- Osterbrock, D. E., & Pogge, R. W. 1985, *ApJ*, 297, 166
- Owsianik, I., Conway, J. E., & Polatidis, A. G. 1998, *A&A*, 336, L37
- Padovani, P., Alexander, D. M., Assef, R. J., et al. 2017, *A&ARv*, 25, 2
- Peck, A. B., & Taylor, G. B. 2000, *ApJ*, 534, 90
- Polatidis, A. G., & Conway, J. E. 2003, *Publ. Astron. Soc. Australia*, 20, 69
- Randall, K. E., Hopkins, A. M., Norris, R. P., & Edwards, P. G. 2011, *MNRAS*, 416, 1135
- Rawlings, S., & Saunders, R. 1991, *Nature*, 349, 138
- Richards, J. L., & Lister, M. L. 2015, *ApJ*, 800, L8
- Sánchez-Blázquez, P., Peletier, R. F., Jiménez-Vicente, J., et al. 2006, *MNRAS*, 371, 703
- Schlegel, D. J., Finkbeiner, D. P., & Davis, M. 1998, *ApJ*, 500, 525
- Shen Y., Greene J. E., Strauss M. A., Richards G. T., Schneider D. P., 2008, *ApJ*, 680, 169
- Shen, Y., Richards, G. T., Strauss, M. A., et al. 2011, *ApJS*, 194, 45
- Snellen, I. A. G., Lehnert, M. D., Bremer, M. N., & Schilizzi, R. T. 2002, *MNRAS*, 337, 981
- Snellen, I. A. G., Lehnert, M. D., Bremer, M. N., & Schilizzi, R. T. 2003, *MNRAS*, 342, 889
- Snellen, I. A. G., Mack, K.-H., Schilizzi, R. T., & Tschager, W. 2004, *MNRAS*, 348, 227
- Snellen, I. A. G., Schilizzi, R. T., de Bruyn, A. G., et al. 1998, *A&AS*, 131, 435
- Son, D., Woo, J.-H., Kim, S. C., et al. 2012, *ApJ*, 757, 140
- Spencer, R. E., McDowell, J. C., Charlesworth, M., et al. 1989, *MNRAS*, 240, 657
- Stanghellini, C., Dallacasa, D., & Orienti, M. 2009, *Astronomische Nachrichten*, 330, 223
- Stanghellini, C., O’Dea, C. P., Dallacasa, D., et al. 1998, *A&AS*, 131, 303
- Sulentic, J. W., Bachev, R., Marziani, P., Negrete, C. A., & Dultzin, D. 2007, *ApJ*, 666, 757
- Tody, D. 1986, *Proc. SPIE*, 627, 733
- Tody, D. 1993, *Astronomical Data Analysis Software and Systems II*, 52, 173
- Tremaine, S., Gebhardt, K., Bender, R., et al. 2002, *ApJ*, 574, 740
- Ulvestad, J. S., Antonucci, R. R. J., & Barvainis, R. 2005, *ApJ*, 621, 123
- Vazdekis, A., Sánchez-Blázquez, P., Falcón-Barroso, J., et al. 2010, *MNRAS*, 404, 1639
- Véron-Cetty M.-P., Véron P., Gonçalves A. C., 2001, *A&A*, 372, 730
- Vestergaard, M., & Peterson, B. M. 2006, *ApJ*, 641, 689
- Wang, J., & Wei, J. Y. 2009, *ApJ*, 696, 741
- Wołowska, A., Kunert-Bajraszewska, M., Mooley, K., & Hallinan, G. 2017, *Frontiers in Astronomy and Space Sciences*, 4, 38
- Wu, Q. 2009, *MNRAS*, 398, 1905
- Xiao, T., Barth, A. J., Greene, J. E., et al. 2011, *ApJ*, 739, 28
- Xu, C., Livio, M., & Baum, S. 1999, *AJ*, 118, 1169
- Yuan, W., Zhou, H. Y., Komossa, S., et al. 2008, *ApJ*, 685, 801-827
- Zhou, H., Wang, T., Yuan, W., et al. 2006, *ApJS*, 166, 128

This paper has been typeset from a \LaTeX file prepared by the author.

Table 1. Sample

SDSS name (1)	z (2)	type (3)	refs. (4)	ID (5)	$P_{5\text{GHz}}$ (6)	refs. (7)	LS (8)	refs. (9)	$\log M_{\text{BH}}$ (10)	method (11)	$\log L_{\text{bol}}$ (12)	method (13)	$\log R_{\text{edd}}$ (14)	S/N (15)
J002225.42+001456.1	0.306	GPS	S98	G	26.52	O98	0.27	O98	8.55	[O III]	43.73	[O III]	-2.96	7.2
J002833.42+005510.9	0.104	CSS	K10	G	24.35	K10	3.35	K10	7.47	σ_*	45.13	[O III]	-1.48	20.9
J002914.24+345632.2	0.517	CSO	A12	G	27.13	H04	0.20	A12	8.57	[O III]	43.91	[O III]	-2.80	3.0
J005905.51+000651.6	0.719	CSS	E04	Q	27.50	L97	8.32	H β	45.73	H β + Mg II	-0.72	25.7
J014109.16+135328.3	0.621	CSS	S89	Q	27.16	O98	6.25	O98	8.59	[O III]	44.67	[O III]	-2.05	2.9
J074417.47+375317.2	1.066	CSS	S89	Q	27.26	O98	17.87	O98	9.11	Mg II	45.99	Mg II	-1.26	28.8
J075303.33+423130.8	3.594	CSO	T20	Q	28.68	H07	8.35	C IV	46.86	C IV	0.37	35.3
J075448.84+303355.0 ^a	0.796	HFP	S09	Q	26.74	S09	9.20	Mg II	45.93	Mg II	-1.41	21.3
J075756.71+395936.1	0.066	CSS	K10	G	23.50	K10	0.25	K10	7.69	σ_*	43.87	[O III]	-1.97	28.0
J080133.55+141442.8	1.196	CSS	S89	Q	27.86	O98	33.99	O98	8.82	Mg II	45.63	Mg II	-1.33	6.7
J080413.88+470442.8	0.510	CSS	F01	Q	26.52	K10	6.18	K10	8.64	Mg II	44.93	Mg II	-1.85	5.0
J080442.23+301237.0	1.450	CSS	K02	Q	27.72	K10	10.98	K10	8.97	Mg II	45.97	Mg II + C IV	-1.13	27.4
J080447.96+101523.7	1.968	CSS	S89	Q	28.12	O98	31.02	O98	8.06	C IV	46.45	C IV	0.25	24.2
J081253.10+401859.9	0.551	CSS	F01	Q	26.73	K10	7.72	K10	8.05	[O III]	44.94	[O III]	-1.25	4.6
J081323.75+073405.6	0.112	CSS	K10	G	24.71	K10	2.81	K10	8.37	σ_*	43.58	[O III]	-2.93	20.3
J082504.56+315957.0	0.265	CSS	K10	G	24.82	K10	7.75	K10	9.66	σ_*	10.6
J083139.79+460800.8	0.131	GPS	S04	G	24.65	D09	0.02	D09	9.19	σ_*	43.29	[O III]	-4.04	26.0
J083411.09+580321.4	0.093	GPS	SW98	G	24.13	B91	8.6e-3*	S03	8.83	σ_*	15.3
J083637.84+440109.6	0.055	CSS	S04	G	23.66	D09	1.72	D09	8.62	σ_*	43.44	[O III]	-3.32	29.0
J083825.00+371036.5	0.396	CSS	K10	G	25.92	K10	1.02	K10	9.26	[O III]	43.76	[O III]	-3.63	2.9
J084856.57+013647.8	0.350	CSS	K10	Q	25.15	K10	6.16	K10	8.41	[O III]	44.41	[O III]	-2.14	2.9
J085314.22+021453.8	0.459	CSS	K10	G	25.42	K10	6.01	K10	2.1
J085408.44+021316.1	0.459	CSS	K10	G	25.34	K10	3.43	K10	1.6
J085601.22+285835.4	1.084	CSS	K02	Q	27.09	K10	6.53	K10	8.67	Mg II	45.43	Mg II	-1.37	10.1
J090105.25+290146.9	0.194	CSS	S89	G	25.96	O98	19.33	O98	7.83	σ_*	43.77	[O III]	-2.20	11.8
J090615.53+463619.0	0.085	GPS	S04	G	24.49	D09	0.05	D09	8.91	σ_*	43.28	[O III]	-3.77	35.0
J090933.49+425346.5	0.670	CSS	S89	G	27.23	O98	56.15	O98	7.5
J091734.79+501638.1	0.632	CSS	K10	Q	25.82	K10	4.87	K10	6.9
J092405.30+141021.4	0.136	CSS	K10	G	24.18	K10	0.74	K10	9.17	σ_*	43.48	[O III]	-3.83	26.4
J092608.00+074526.6	0.442	CSS	K10	Q	25.60	K10	7.98	K10	8.62	H β	44.81	H β	-1.96	22.2
J093430.68+030545.3	0.225	CSS	K10	G	25.25	K10	1.62	K10	9.45	σ_*	43.88	[O III]	-3.71	15.1
J093609.36+331308.3	0.076	GPS	S04	G	23.84	D09	2.2e-3*	D09	8.95	σ_*	43.18	[O III]	-3.92	33.8
J094525.90+352103.6	0.208	CSS	K10	Q	24.72	K10	4.45	K10	7.70	σ_*	44.47	[O III]	-1.37	19.2
J095111.52+345131.9	0.358	HFP	S09	G	25.43	O10	0.02	A12	9.27	[O III]	43.86	[O III]	-3.56	6.1
J095412.57+420109.1	1.787	CSS	F01	Q	27.56	K10	16.89	K10	8.28	C IV	45.49	C IV	-0.82	2.4
J100800.04+073016.6	0.877	CSS	S89	Q	27.88	O98	10.05	O98	9.84	[O III]	45.32	[O III]	-2.66	2.2
J100955.51+140154.2	0.213	CSS	K10	G	25.71	K10	3.29	K10	9.10	σ_*	43.59	[O III]	-3.65	14.1
J101251.77+403903.4	0.506	CSS	K02	G	27.01	K10	32.80	K10	2.3
J101714.23+390121.1	0.211	CSS	F01	G	25.80	K10	20.97	K10	6.3
J102027.20+432056.3	1.962	HFP	S09	Q	27.80	S09	8.72	Mg II	45.95	Mg II + C IV	-0.90	13.5
J102523.78+254158.3	0.457	HFP	S09	G	25.58	S09	9.28	[O III]	44.10	[O III]	-3.32	3.1
J102618.25+454229.3	0.152	CSO	S04	G	24.55	D09	0.04	D09	9.08	σ_*	43.52	[O III]	-3.70	18.1
J102844.26+384436.8	0.362	CSS	F01	Q	26.18	K10	16.17	K10	8.74	σ_*	44.10	[O III]	-2.78	14.6
J103507.04+562846.7	0.460	GPS	S98	Q	27.00	O98	0.23	O98	9.37	[O III]	44.13	[O III]	-3.38	3.1
J103532.58+423019.0	2.432	HFP	S09	Q	27.71	S09	8.93	Mg II	45.86	Mg II + C IV	-1.22	9.1
J103719.33+433515.3	0.025	CSS	S04	G	22.96	D09	9.4e-3	D09	8.77	σ_*	42.58	[O III]	-4.33	54.6
J104029.94+295757.7	0.091	CSS	K10	G	24.34	K10	3.67	K10	8.31	σ_*	43.37	[O III]	-3.08	29.4
J104406.33+295900.9	2.983	HFP	S09	Q	28.14	S09	7.95	C IV	46.15	C IV	0.06	8.9
J105250.06+335504.9	1.405	HFP	S09	Q	26.74	S09	9.53	Mg II	46.43	Mg II	-1.23	27.9
J105628.25+501952.0	0.820	CSS	K10	Q	26.01	K10	8.18	K10	9.23	Mg II	45.76	Mg II	-1.61	22.8
J105731.17+405646.1	0.025	GPS	S04	G	22.60	D09	3e-4*	D09	9.26	σ_*	42.47	[O III]	-4.93	52.7
J112027.80+142055.0	0.363	GPS	S98	Q	26.65	O98	0.40	O98	9.10	[O III]	44.11	[O III]	-3.13	2.5
J113138.89+451451.1	0.398	CSS	F01	Q	26.59	K10	4.88	K10	8.68	[O III]	44.20	[O III]	-2.62	4.7
J114311.02+053516.0	0.497	CSS	K10	Q	25.76	K10	17.03	K10	7.74	H β	44.35	H β + Mg II	-1.53	5.7
J114339.59+462120.4	0.116	CSS	F01	G	24.66	K10	17.06	K10	8.89	σ_*	13.0
J114856.56+525425.2	1.632	HFP	D00	Q	27.84	D00	6.8e-3	A12	8.81	Mg II	46.58	Mg II + C IV	-0.37	33.0
J115000.08+552821.3	0.138	CSS	S04	G	24.57	D09	0.10*	D09	8.9
J115618.74+312804.7	0.417	CSS	S89	Q	26.80	O98	4.96	O98	7.73	H β	44.68	H β + Mg II	-1.19	7.6
J115727.60+431806.3	0.230	CSS	K10	Q	25.22	K10	4.59	K10	7.96	H β	44.72	H β + H α	-1.38	29.7
J115919.97+464545.1	0.467	CSS	K10	G	26.40	K10	5.00	K10	3.0
J120321.93+041419.0	1.224	GPS	S02	Q	27.74	C10	0.60	C10	8.99	Mg II	45.60	Mg II	-1.53	10.3
J120406.82+391218.2	0.445	CSS	F01	G	26.08	K10	12.06	K10	2.4

Table 1. Continued...

SDSS name (1)	z (2)	type (3)	refs. (4)	ID (5)	$P_{5\text{GHz}}$ (6)	refs. (7)	LS (8)	refs. (9)	$\log M_{\text{BH}}$ (10)	method (11)	$\log L_{\text{bol}}$ (12)	method (13)	$\log R_{\text{edd}}$ (14)	S/N (15)
J120624.70+641336.8	0.372	CSS	S89	Q	26.72	O98	6.98	O98	8.24	H α	44.40	H α	-1.97	3.2
J120902.79+411559.2	0.096	CSS	S04	G	24.26	D09	0.04	D09	9.01	σ_*	30.0
J124419.96+405136.8	0.249	CSS	F01	Q	25.51	K10	3.91	K10	8.28	σ_*	44.16	[O III]	-2.25	13.2
J124449.18+404806.2	0.814	CSS	F01	Q	27.35	K10	0.30	K10	8.73	Mg II	44.92	Mg II	-1.95	6.3
J124733.31+672316.4	0.107	CSO	A12	G	24.75	A12	0.02	A12	8.95	σ_*	43.17	[O III]	-3.92	35.0
J125226.35+563419.6	0.320	CSS	S89	Q	26.53	O98	7.78	O98	8.37	H β	45.08	H β + H α	-1.44	14.1
J125325.72+303635.1	1.314	CSS	K02	Q	27.31	K10	4.62	K10	8.30	Mg II	45.00	Mg II	-1.44	6.3
J130941.51+404757.2	2.907	HFP	S09	Q	27.97	O10	0.01	O12	8.07	C IV	46.30	C IV	0.09	18.8
J131057.00+445146.2	0.391	CSS	K10	G	25.26	K10	3.87	K10	5.2
J131718.64+392528.1	1.563	CSS	K02	Q	27.55	K10	0.29	K10	8.65	Mg II	46.06	Mg II + C IV	-0.73	18.1
J131739.20+411545.6	0.066	GPS	S04	G	24.37	D09	5.1e-3	D09	8.84	σ_*	42.68	[O III]	-4.30	28.1
J132255.66+391208.0	2.987	HFP	S09	Q	28.22	S09	8.81	C IV	46.90	C IV	-0.05	30.1
J132419.67+041907.0	0.263	CSS	K10	G	24.99	K10	17.04	K10	6.2
J132513.37+395553.2	0.076	GPS	S04	G	23.36	D09	0.01	D09	8.84	σ_*	42.98	[O III]	-4.00	34.2
J133037.69+250910.9	1.055	CSS	S89	Q	28.28	O98	0.39	O98	8.38	Mg II	45.79	Mg II	-0.73	17.7
J133108.29+303032.9	0.850	CSS	S89	Q	28.41	O98	24.51	O98	8.14	H β	45.58	H β + Mg II	-0.70	37.3
J134035.20+444817.3	0.065	GPS	S04	G	23.89	D09	4.1e-3	D09	7.32	σ_*	43.49	[O III]	-1.96	20.0
J134536.94+382312.5	1.852	CSS	F01	Q	27.98	K10	0.93	K10	9.41	Mg II	46.48	Mg II + C IV	-1.07	22.6
J134733.36+121724.2	0.120	GPS	S98	Q	26.06	O98	0.17	O98	8.63	σ_*	43.84	[O III]	-2.93	17.9
J140028.65+621038.5	0.429	GPS	S89	Q	27.08	O98	0.39	O98	8.55	[O III]	44.26	[O III]	-2.43	3.4
J140051.58+521606.5	0.118	CSS	K10	G	24.36	K10	0.32*	K09	8.87	σ_*	43.13	[O III]	-3.88	22.0
J140319.30+350813.3	2.291	CSS	K02	Q	26.12	K10	10.21	K10	8.99	Mg II	45.63	Mg II + C IV	-1.50	8.2
J140416.35+411748.7	0.360	CSS	K10	G	25.51	K10	1.01	K10	2.6
J140700.39+282714.6	0.077	GPS	S98	Q	25.59	O98	0.01	O98	8.72	H β	44.89	H β + H α	-1.97	47.5
J140909.50+364208.1	2.241	CSS	K02	Q	27.04	K10	1.98	K10	8.54	Mg II	45.24	Mg II + C IV	-1.44	3.6
J140942.44+360415.9	0.149	CSS	K10	Q	24.42	K10	0.07	K10	7.92	σ_*	43.83	[O III]	-2.22	10.2
J141327.22+550529.2	0.282	CSS	K10	G	24.92	K10	0.81	K10	8.9
J141414.83+455448.7	0.458	CSO	A12	G	26.22	A12	0.17	A12	2.9
J141558.81+132023.7	0.247	CSO	A12	G	26.19	A12	0.03	A12	5.3
J141908.18+062834.7	1.436	CSS	S89	Q	28.28	O98	12.58	O98	8.95	Mg II	46.40	Mg II	-0.69	33.0
J142051.48+270427.0	2.516	HFP	S09	Q	27.73	O10	8.62	C IV	46.05	C IV	-0.71	4.5
J142104.24+050844.7	0.445	CSS	K10	G	25.91	K10	1.68	K10	3.1
J142123.06+464547.9	1.668	HFP	S09	Q	27.52	S09	8.94	Mg II	46.07	Mg II + C IV	-1.01	13.6
J143009.74+104326.9	1.705	HFP	D00	Q	28.25	D00	8.69	Mg II	46.03	Mg II + C IV	-0.79	14.0
J143521.67+505122.9	0.100	CSS	S04	G	24.20	D09	0.28*	D09	8.32	σ_*	42.91	[O III]	-3.55	17.5
J144516.46+095836.0	3.541	GPS	S98	Q	29.14	O98	0.15	O98	9.03	C IV	46.59	C IV	-0.57	31.0
J144712.76+404744.9	0.195	CSS	F01	G	25.23	K10	26.28	K10	8.81	σ_*	43.36	[O III]	-3.59	11.1
J145958.43+333701.8	0.644	HFP	S09	Q	26.53	S09	8.98	H β	46.06	H β + Mg II	-1.06	31.6
J150426.69+285430.5	2.285	CSS	K02	Q	28.02	K10	0.35	K10	8.41	Mg II	46.14	Mg II + C IV	-0.42	23.8
J151141.26+051809.2	0.084	HFP	D00	Q	24.97	D00	7.6e-3	A12	7.88	σ_*	43.79	[O III]	-2.23	29.6
J152005.47+201605.4	1.572	CSS	S89	Q	28.11	O98	8.90	O98	8.75	Mg II	45.49	Mg II + C IV	-1.40	9.9
J152349.34+321350.2	0.110	CSS	K10	G	24.20	K10	0.40	K10	7.79	σ_*	43.60	[O III]	-2.34	17.5
J152837.01+381605.9	0.749	HFP	S09	Q	26.11	S09	7.83	Mg II	44.55	Mg II	-1.42	2.2
J153409.90+301204.0	0.929	CSS	K10	Q	19.80	K10	4e-3	K10	2.6
J154349.50+385601.3	0.553	CSS	K10	Q	25.77	K10	8.10	K10	8.76	[O III]	44.42	[O III]	-2.48	2.6
J154525.48+462244.3	0.525	CSS	K10	Q	25.79	K10	6.59	K10	9.76	[O III]	44.89	[O III]	-3.01	3.1
J154609.52+002624.6	0.558	GPS	S02	G	27.02	L07	0.04	A12	9.13	[O III]	44.31	[O III]	-2.96	2.9
J154754.12+351842.2	0.620	HFP	S09	Q	25.90	S09	7.85	Mg II	44.47	Mg II	-1.51	1.9
J155235.38+441905.9	0.452	CSS	K10	G	25.56	K10	6.93	K10	2.6
J155927.67+533054.4	0.179	CSS	K10	G	24.72	K10	5.13	K10	8.34	σ_*	43.73	[O III]	-2.74	25.0
J160239.62+264606.0	0.371	HFP	S09	Q	25.82	S09	9.66	[O III]	44.22	[O III]	-3.58	3.1
J160246.39+524358.3	0.106	CSS	K10	G	24.77	K10	0.38	K10	8.69	σ_*	43.22	[O III]	-3.61	26.4
J160335.16+380642.8	0.241	CSS	K02	G	27.03	K10	6.09	K10	9.26	[O III]	43.61	[O III]	-3.79	7.6
J160913.32+264129.0	0.474	GPS	S89	Q	27.16	O98	0.30	O98	9.03	[O III]	44.61	[O III]	-2.57	3.0
J161148.52+404020.9	0.151	CSS	K10	Q	25.01	K10	2.63	K10	8.39	σ_*	43.95	[O III]	-2.58	14.0
J161748.41+380141.8	1.609	HFP	S09	Q	27.10	S09	9.10	Mg II	45.79	Mg II + C IV	-1.45	8.2
J161823.57+363201.7	0.733	CSS	K02	G	26.82	K10	0.44	K10	16.0
J162111.27+374604.9	1.271	CSS	K02	Q	27.27	K10	6.28	K10	8.68	Mg II	45.30	Mg II	-1.53	8.4
J163402.95+390000.5	1.083	CSS	K02	Q	27.38	K10	6.53	K10	8.29	Mg II	45.29	Mg II	-1.13	13.7
J164311.34+315618.4	0.587	CSS	K10	Q	25.76	K10	10.58	K10	8.31	H β	44.96	H β + Mg II	-1.49	9.4
J164348.60+171549.4	0.163	CSS	S89	G	25.99	O98	22.40	O98	8.67	σ_*	43.44	[O III]	-3.36	25.3
J165822.18+390625.6	0.425	CSS	K02	G	27.10	K10	0.97	K10	2.3

Table 1. Continued...

SDSS name (1)	z (2)	type (3)	refs. (4)	ID (5)	$P_{5\text{GHz}}$ (6)	refs. (7)	LS (8)	refs. (9)	$\log M_{\text{BH}}$ (10)	method (11)	$\log L_{\text{bol}}$ (12)	method (13)	$\log R_{\text{edd}}$ (14)	S/N (15)
J213638.58+004154.2	1.941	GPS	S98	Q	29.36	O98	0.02	O98	8.78	Mg II	46.76	Mg II + C IV	-0.15	32.9
J225025.34+141952.0	0.235	CSS	S89	Q	26.30	O98	0.75	O98	7.75	H β	44.74	H β + H α	-1.14	35.6
object name (1)	z (2)	type (3)	refs. (4)	ID (5)	$P_{5\text{GHz}}$ (6)	refs. (7)	LS (8)	refs. (9)	$\log M_{\text{BH}}$ (10)	method (11)	$\log L_{\text{bol}}$ (12)	method (13)	$\log R_{\text{edd}}$ (14)	S/N (15)
HB89 1127-145	1.184	GPS	S98	Q	28.48	O98	0.03	O98	8.78	Mg II	46.48	Mg II	-0.41	32.9
CGRaBS J1424+2256	3.620	GPS	S98	Q	28.87	D00	9.55	C IV	47.97	C IV	0.3	32.9

Columns are listed as follows: (1) object name; (2) redshift; (3) - (4) type and the reference; (5) source classification: G - galaxy, Q - quasar; (6) - (7) radio power at 5 GHz and the reference; (8) - (9) linear size and the reference; (10) black hole mass; (11) adopted method in estimating the black hole mass; (12) bolometric luminosity; (13) adopted method in estimating the bolometric luminosity; (14) Eddington ratio ($L_{\text{bol}}/L_{\text{edd}}$); (15) median signal-to-noise ratio of the spectrum.

References: A12: [An & Baan \(2012\)](#); B91: [Becker et al. \(1991\)](#); C10: [Cui et al. \(2010\)](#); D00: [Dallacasa et al. \(2000\)](#); D09: [de Vries et al. \(2009\)](#); E04: [Edwards & Tingay \(2004\)](#); F01: [Fanti et al. \(2001\)](#); H04: [Horiuchi et al. \(2004\)](#); H07: [Helmboldt et al. \(2007\)](#); K02: [Kunert et al. \(2002\)](#); K10: [Kunert-Bajraszewska et al. \(2010\)](#); L97: [Laurent-Muehleisen et al. \(1997\)](#); L07: [Labiano et al. \(2007\)](#); O98: [O'Dea \(1998\)](#); O10: [Orienti et al. \(2010\)](#); O12: [Orienti & Dallacasa \(2012\)](#); S89: [Spencer et al. \(1989\)](#); S98: [Stanghellini et al. \(1998\)](#); SW98: [Snellen et al. \(1998\)](#); S02: [Snellen et al. \(2002\)](#); S03: [Snellen et al. \(2003\)](#); S04: [Snellen et al. \(2004\)](#); S09: [Stanghellini et al. \(2009\)](#); T20: [Peck & Taylor \(2000\)](#)

*: the upper limit of linear size

Table 2. Emission line properties

SDSS name (1)	C IV (2)	(3)	Mg II (4)	(5)	H β (6)	(7)	[O III] (8)	(9)	H α (10)	(11)	[S II] (12)	(13)
J002225.42+001456.1	484 \pm 31	43 \pm 2	401 \pm 90	13 \pm 4
J002833.42+005510.9	219 \pm 13	1472 \pm 22	452 \pm 7	532 \pm 8
J002914.24+345632.2	491 \pm 57	21 \pm 2
J005905.51+000651.6	3771 \pm 336	1477 \pm 46	2567 \pm 376	884 \pm 60	982 \pm 52	600 \pm 74
J014109.16+135328.3	494 \pm 0	115 \pm 2
J074417.47+375317.2	6600 \pm 300	975 \pm 19
J075303.33+423130.8	2944 \pm 55	686 \pm 29
J075448.84+303355.0	7554 \pm 655	1732 \pm 62
J075756.71+395936.1	276 \pm 8	1860 \pm 17	351 \pm 9	338 \pm 8
J080133.55+141442.8	5946 \pm 765	324 \pm 9
J080413.88+470442.8	7639 \pm 712	518 \pm 35	597 \pm 5	852 \pm 4
J080442.23+301237.0	4396 \pm 385	785 \pm 73	5533 \pm 333	473 \pm 10
J080447.96+101523.7	2789 \pm 686	1146 \pm 56
J081253.10+401859.9	374 \pm 11	331 \pm 14
J081323.75+073405.6	518 \pm 45	265 \pm 15	558 \pm 12	445 \pm 8
J082504.56+315957.0
J083139.79+460800.8	682 \pm 105	85 \pm 12	385 \pm 33	72 \pm 9
J083411.09+580321.4	490 \pm 93	63 \pm 6
J083637.84+440109.6	333 \pm 0	793 \pm 0	595 \pm 0	355 \pm 0
J083825.00+371036.5	703 \pm 63	26 \pm 2
J084856.57+013647.8	450 \pm 11	215 \pm 3	485 \pm 42	53 \pm 7
J085314.22+021453.8
J085408.44+021316.1
J085601.22+285835.4	5684 \pm 529	260 \pm 14
J090105.25+290146.9	698 \pm 94	140 \pm 67	573 \pm 51	54 \pm 7
J090615.53+463619.0	541 \pm 88	212 \pm 84	2322 \pm 55	1437 \pm 74	518 \pm 17	405 \pm 11
J090933.49+425346.5
J091734.79+501638.1
J092405.30+141021.4	771 \pm 54	134 \pm 5	756 \pm 29	356 \pm 8
J092608.00+074526.6	4475 \pm 719	111 \pm 26	7062 \pm 320	354 \pm 14	308 \pm 3	496 \pm 4
J093430.68+030545.3	569 \pm 21	134 \pm 4	586 \pm 32	120 \pm 4
J093609.36+331308.3	558 \pm 75	197 \pm 62	454 \pm 23	205 \pm 10
J094525.90+352103.6	277 \pm 8	835 \pm 10	3033 \pm 103	928 \pm 29	327 \pm 23	52 \pm 4
J095111.52+345131.9	709 \pm 0	44 \pm 1
J095412.57+420109.1	6488 \pm 1069	203 \pm 10
J100800.04+073016.6	1985 \pm 186	43 \pm 4	956 \pm 0	305 \pm 4
J100955.51+140154.2	618 \pm 59	68 \pm 5	774 \pm 87	106 \pm 21
J101251.77+403903.4
J101714.23+390121.1
J102027.20+432056.3	2847 \pm 161	383 \pm 43	4358 \pm 397	186 \pm 9
J102523.78+254158.3	710 \pm 28	48 \pm 2	555 \pm 119	26 \pm 5
J102618.25+454229.3	637 \pm 128	117 \pm 7	773 \pm 149	52 \pm 10
J102844.26+384436.8	544 \pm 18	84 \pm 2	662 \pm 34	64 \pm 3
J103507.04+562846.7	748 \pm 12	53 \pm 1
J103532.58+423019.0	5907 \pm 255	208 \pm 25	6599 \pm 244	62 \pm 6
J103719.33+433515.3	443 \pm 61	376 \pm 109	456 \pm 19	741 \pm 26
J104029.94+295757.7	687 \pm 31	231 \pm 9	727 \pm 42	378 \pm 19
J104406.33+295900.9	3021 \pm 166	210 \pm 32
J105250.06+335504.9	7929 \pm 498	1374 \pm 53
J105628.25+501952.0	8762 \pm 641	1110 \pm 49

Table 2. Continued...

SDSS name (1)	C IV (2)	(3)	Mg II (4)	(5)	H β (6)	(7)	[O III] (8)	(9)	H α (10)	(11)	[S II] (12)	(13)
J105731.17+405646.1	560 \pm 39	266 \pm 18	532 \pm 53	264 \pm 23
J112027.80+142055.0	648 \pm 22	86 \pm 3	993 \pm 128	29 \pm 6
J113138.89+451451.1	518 \pm 35	64 \pm 8	2565 \pm 93	225 \pm 12	991 \pm 110	55 \pm 8
J114311.02+053516.0	6971 \pm 1280	100 \pm 21	3150 \pm 347	139 \pm 13	767 \pm 9	527 \pm 6
J114339.59+462120.4	450 \pm 22	146 \pm 6
J114856.56+525425.2	5036 \pm 152	2625 \pm 62	3289 \pm 373	1128 \pm 49
J115000.08+552821.3	479 \pm 30	28 \pm 2
J115618.74+312804.7	4541 \pm 553	548 \pm 46	3045 \pm 341	227 \pm 12	528 \pm 23	875 \pm 14
J115727.60+431806.3	3296 \pm 307	1592 \pm 74	331 \pm 3	1051 \pm 8	3067 \pm 48	4369 \pm 36	333 \pm 13	66 \pm 3
J115919.97+464545.1
J120321.93+041419.0	7404 \pm 910	283 \pm 19
J120406.82+391218.2
J120624.70+641336.8	725 \pm 0	513 \pm 2	7569 \pm 157	739 \pm 10	993 \pm 23	61 \pm 4
J120902.79+411559.2
J124419.96+405136.8	370 \pm 63	237 \pm 79	2595 \pm 140	927 \pm 50	605 \pm 112	112 \pm 12
J124449.18+404806.2	8604 \pm 983	162 \pm 14	763 \pm 28	114 \pm 4
J124733.31+672316.4	548 \pm 49	94 \pm 8	476 \pm 42	62 \pm 4
J125226.35+563419.6	4431 \pm 670	1334 \pm 208	525 \pm 4	2774 \pm 20	3981 \pm 219	5025 \pm 147	517 \pm 31	233 \pm 16
J125325.72+303635.1	4955 \pm 548	59 \pm 10
J130941.51+404757.2	3138 \pm 201	313 \pm 34
J131057.00+445146.2
J131718.64+392528.1	6682 \pm 636	981 \pm 100	4177 \pm 255	293 \pm 11
J131739.20+411545.6	514 \pm 78	65 \pm 9	555 \pm 79	141 \pm 19
J132255.66+391208.0	4861 \pm 59	1165 \pm 76
J132419.67+041907.0	466 \pm 84	57 \pm 7
J132513.37+395553.2	541 \pm 38	114 \pm 17	653 \pm 32	291 \pm 16
J133037.69+250910.9	3236 \pm 206	639 \pm 19
J133108.29+303032.9	2832 \pm 93	478 \pm 13	2074 \pm 201	617 \pm 59	567 \pm 26	371 \pm 35
J134035.20+444817.3	193 \pm 4	660 \pm 7	207 \pm 5	246 \pm 5
J134536.94+382312.5	4416 \pm 276	1617 \pm 288	7325 \pm 377	565 \pm 21
J134733.36+121724.2	1589 \pm 83	413 \pm 37	457 \pm 25	481 \pm 40	2771 \pm 19	4645 \pm 110	589 \pm 18	618 \pm 10
J140028.65+621038.5	484 \pm 18	87 \pm 2	430 \pm 147	18 \pm 5
J140051.58+521606.5	669 \pm 66	69 \pm 7	750 \pm 94	124 \pm 16
J140319.30+350813.3	11872 \pm 1580	109 \pm 5	6875 \pm 761	78 \pm 13
J140416.35+411748.7
J140700.39+282714.6	7659 \pm 255	19313 \pm 253	547 \pm 13	2794 \pm 51	9256 \pm 609	75700 \pm 1128	433 \pm 30	579 \pm 53
J140909.50+364208.1	1821 \pm 150	32 \pm 3	4788 \pm 858	47 \pm 5
J140942.44+360415.9	465 \pm 33	298 \pm 10	489 \pm 47	108 \pm 6
J141327.22+550529.2
J141414.83+455448.7
J141558.81+132023.7
J141908.18+062834.7	4179 \pm 186	1207 \pm 32
J142051.48+270427.0	7011 \pm 317	252 \pm 17
J142104.24+050844.7
J142123.06+464547.9	6275 \pm 394	883 \pm 132	5975 \pm 0	228 \pm 0
J143009.74+104326.9	5868 \pm 363	754 \pm 34	4481 \pm 465	212 \pm 16
J143521.67+505122.9	469 \pm 44	53 \pm 5	510 \pm 32	101 \pm 6
J144516.46+095836.0	7728 \pm 207	388 \pm 26
J144712.76+404744.9	870 \pm 175	43 \pm 6
J145958.43+333701.8	4596 \pm 304	4064 \pm 64	4326 \pm 136	2461 \pm 34	396 \pm 12	338 \pm 7

Table 2. Continued...

SDSS name (1)	C IV		Mg II		H β		[O III]		H α		[S II]	
(1)	(2)	(3)	(4)	(5)	(6)	(7)	(8)	(9)	(10)	(11)	(12)	(13)
J150426.69+285430.5	3041 \pm 52	482 \pm 9	3167 \pm 147	117 \pm 6
J151141.26+051809.2	2483 \pm 112	533 \pm 28	223 \pm 9	898 \pm 23	2799 \pm 47	4213 \pm 201	455 \pm 17	289 \pm 10
J152005.47+201605.4	4222 \pm 850	220 \pm 14	5992 \pm 930	121 \pm 7
J152349.34+321350.2	399 \pm 25	292 \pm 17	420 \pm 25	70 \pm 4
J152837.01+381605.9	3854 \pm 199	85 \pm 4	324 \pm 45	17 \pm 2
J153409.90+301204.0
J154349.50+385601.3	541 \pm 27	76 \pm 3
J154525.48+462244.3	918 \pm 0	321 \pm 3	992 \pm 0	115 \pm 16
J154609.52+002624.6	659 \pm 40	54 \pm 3
J154754.12+351842.2	4155 \pm 298	113 \pm 5	374 \pm 30	22 \pm 1
J155235.38+441905.9
J155927.67+533054.4	519 \pm 27	149 \pm 4	550 \pm 33	71 \pm 4
J160239.62+264606.0	871 \pm 0	111 \pm 4
J160246.39+524358.3	553 \pm 67	111 \pm 8	2724 \pm 191	690 \pm 111	992 \pm 58	185 \pm 16
J160335.16+380642.8	705 \pm 0	54 \pm 2	935 \pm 96	81 \pm 15
J160913.32+264129.0	625 \pm 18	145 \pm 2	3763 \pm 864	212 \pm 11	993 \pm 160	28 \pm 5.1
J161148.52+404020.9	313 \pm 17	394 \pm 14	609 \pm 21	388 \pm 8
J161748.41+380141.8	8309 \pm 2061	446 \pm 79	7780 \pm 738	191 \pm 13
J161823.57+363201.7
J162111.27+374604.9	6320 \pm 844	128 \pm 13
J163402.95+390000.5	4028 \pm 621	189 \pm 15
J164311.34+315618.4	5187 \pm 709	344 \pm 49	4187 \pm 281	303 \pm 18	313 \pm 4	790 \pm 8
J164348.60+171549.4	683 \pm 65	81 \pm 17	482 \pm 56	23 \pm 3
J165822.18+390625.6
J213638.58+004154.2	4280 \pm 138	3138 \pm 59	3325 \pm 345	629 \pm 31
J225025.34+141952.0	2882 \pm 241	1073 \pm 63	512 \pm 10	1451 \pm 31	2990 \pm 88	4910 \pm 142	473 \pm 35	136 \pm 12
SDSS name (1)	C IV		Mg II		H β		[O III]		H α		[S II]	
(1)	(2)	(3)	(4)	(5)	(6)	(7)	(8)	(9)	(10)	(11)	(12)	(13)
HB89 1127 – 145	3677 \pm 370	1607 \pm 78
CGRaBS J1424+2256	5461 \pm 172	9299 \pm 101

Columns: (1) object name; (2) - (3) the FWHM and flux for broad C IV; (4) - (5) the FWHM and flux for broad Mg II; (6) - (7) the FWHM and flux for broad H β ; (8) - (9) the FWHM and flux for [O III] line core; (10) - (11) the FWHM and flux for broad H α ; (12) - (13) the FWHM and flux for [S II] λ 6716. The FWHM and flux are in units of km s $^{-1}$, and 10 $^{-17}$ erg s $^{-1}$ cm $^{-2}$, respectively.

Table 3. The optical variability

SDSS name (1)	type (2)	z (3)	plate (4)	MJD (5)	fiber (6)	S/N (7)	Δf (8)	$\Delta\alpha$ (9)	α_λ (10)	FWHM (C IV) (11)	f (C IV) (12)	FWHM (Mg II) (13)	f (Mg II) (14)
J075303.33+423130.8	CSO	3.593	434	51885	71	23.6	47.0	BWB	-1.62 \pm 0.06	2711 \pm 57	532 \pm 48
			3683	55245	488	29.1			-1.95 \pm 0.02	2944 \pm 61	651 \pm 72		
J080442.23+301237.0	CSS	1.448	860	52319	495	26.1	1.2		-1.83 \pm 0.35	5207 \pm 107	447 \pm 8
			4451	55537	546	27.4			-1.27 \pm 0.16	5098 \pm 423	491 \pm 70
J085601.22+285835.4	CSS	1.084	1589	52972	37	9.3	4.7		-1.94 \pm 0.28	5489 \pm 938	300 \pm 65
			1934	53357	386	10.1			-1.85 \pm 0.46	6014 \pm 1087	294 \pm 56
J102027.20+432056.3	HFP	1.964	1218	52709	607	8.4	20.0	BWB	-0.45 \pm 0.03	2537 \pm 191	568 \pm 77	4632 \pm 650	165 \pm 10
			3287	54941	483	13.5			-0.15 \pm 0.02	2886 \pm 144	347 \pm 33	4245 \pm 336	166 \pm 7
J103532.58+423019.0	HFP	2.432	1360	53033	562	8.4	36.0		-0.90 \pm 0.03	6081 \pm 270	326 \pm 39
			4632	55644	738	9.1			-0.96 \pm 0.03	5926 \pm 238	211 \pm 33
J104406.33+295900.9	HFP	2.981	1969	53383	48	7.4	50.0	BWB	-1.40 \pm 0.06	3428 \pm 131	526 \pm 64
			6452	56366	946	8.9			-1.09 \pm 0.03	3021 \pm 173	209 \pm 24
J105628.25+501952.0	CSS	0.820	876	52346	112	22.8	19.0		-1.43 \pm 0.03	7156 \pm 127	1074.4 \pm 21.7
			876	52669	112	21.7			-1.37 \pm 0.26	7499 \pm 340	1127 \pm 93
J130941.51+404757.2	HFP	2.908	1460	53138	267	7.6	60.0	BWB	-1.13 \pm 0.05	3273 \pm 194	285 \pm 45
			4706	55705	768	18.8			-1.23 \pm 0.01	3157 \pm 125	326 \pm 28
J132255.66+391208.0	HFP	2.990	1977	53475	496	24.5	15.0		-1.18 \pm 0.02	4784 \pm 85	1112 \pm 84
			3984	55333	548	30.1			-1.32 \pm 0.01	4842 \pm 60	1112 \pm 75
J133108.29+303032.9	CSS	0.849	2110	53467	104	26.0	4.9		-1.64 \pm 0.66	2865 \pm 344	639 \pm 91
			6491	56337	596	37.3			-1.84 \pm 0.23	2944 \pm 109	600 \pm 15
J134536.94+382312.5	CSS	1.852	2014	53460	271	15.4	37.0	BWB	-0.70 \pm 0.02	4997 \pm 290	1440 \pm 142	6160 \pm 264	463 \pm 11
			3987	55590	958	22.6			-0.98 \pm 0.01	4977 \pm 211	1834 \pm 150	6452 \pm 241	599 \pm 11
J144516.46+095836.0	GPS	3.520	1713	53827	314	19.0	18.0		-1.85 \pm 0.07	7921 \pm 349	499 \pm 51
			5472	55976	822	31.0			-2.34 \pm 0.02	8076 \pm 251	597 \pm 48
J150426.69+285430.5	CSS	2.282	2151	54523	426	12.7	2.1		-1.34 \pm 0.02	3118 \pm 86	598 \pm 55
			3877	55365	818	23.8			-0.89 \pm 0.01	3002 \pm 45	482 \pm 9
SDSS name (1)	type (2)	z (3)	plate (4)	MJD (5)	fiber (6)	S/N (7)	Δf (8)	$\Delta\alpha$ (9)	α_λ (10)	FWHM (C IV) (11)	f (C IV) (12)	FWHM (H β) (13)	f (H β) (14)
J092608.00+074526.6	CSS	0.442	1195	52724	453	10.8	7.0		-0.05 \pm 0.02	7387 \pm 622	650 \pm 24
			2402	54176	484	22.2			-0.17 \pm 0.01	7560 \pm 453	705 \pm 16
J115727.60+431806.3	CSS	0.230	1447	53120	571	15.8	41.0	BWB	-0.60 \pm 0.44	3468 \pm 656	1368 \pm 432
			6642	56396	248	29.7			-1.24 \pm 0.50	3370 \pm 588	1751 \pm 429

Columns: (1) object name; (2) source type; (3) redshift; (4) - (6) the plate, MJD, and fiber of spectroscopic observations; (7) median signal-to-noise ratio of the spectrum; (8) the variability in % (see text for details); (9) color variation: BWB - bluer-when-brighter; (10) the spectral index of power-law continuum; (11) - (12) the FWHM and flux of C IV in units of km s⁻¹, and 10⁻¹⁷erg s⁻¹cm⁻², respectively; (13) - (14) same as (11) - (12) but for broad Mg II or broad H β .

Table 4. Radio and spectroscopic classification

SDSS name	type	type	SN	H β $\lambda 4861$	[O III] $\lambda 5007$	[O I] $\lambda 6300$	H α $\lambda 6563$	[N II] $\lambda 6584$	[S II] $\lambda 6717$	[S II] $\lambda 6731$	EI	HEG/LEG	log R_{edd}	Type1/Type2
(1)	(2)	(3)	(4)	(5)	(6)	(7)	(8)	(9)	(10)	(11)	(12)	(13)	(14)	(15)
J002833.42+005510.9	CSS	G	21	165	1472	224	873	1411	532	443	1.06	HEG	-1.48	Type2
J075756.71+395936.1	CSS	G	28	203	1860	126	1038	940	338	292	1.35	HEG	-1.97	Type2
J081323.75+073405.6	CSS	G	20	106	265	192	639	1071	445	393	0.46	LEG	-2.93	Type2
J083139.79+460800.8	GPS	G	26	24	85	30	117	131	72	63	0.72	LEG	-4.04	Type2
J083637.84+440109.6	CSS	G	29	119	793	139	643	835	355	327	1.00	HEG	-3.32	Type2
J090615.53+463619.0	GPS	G	35	184	212	400	399	283	405	315	0.03	LEG	-3.77	Type1 ^a
J092405.30+141021.4	CSS	G	26	128	134	186	518	736	356	327	0.08	LEG	-3.83	Type2
J093430.68+030545.3	CSS	G	15	43	134	53	239	367	120	124	0.64	LEG	-3.71	Type2
J093609.36+331308.3	GPS	G	34	89	197	128	372	425	205	164	0.48	LEG	-3.92	Type2
J100955.51+140154.2	CSS	G	14	39	68	54	195	251	106	116	0.37	LEG	-3.65	Type2
J102523.78+254158.3	HFP	G	3	11	48	26	51	76	26	26	0.67	LEG	-3.32	Type2
J102618.25+454229.3	CSO	G	18	30	117	63	116	156	52	68	0.63	LEG	-3.70	Type2
J102844.26+384436.8	CSS	Q	15	25	84	38	116	158	64	53	0.64	LEG	-2.78	Type2
J103719.33+433515.3	CSS	G	55	223	376	171	915	1635	741	585	0.33	LEG	-4.33	Type2
J104029.94+295757.7	CSS	G	29	80	231	127	530	1197	378	296	0.51	LEG	-3.08	Type2
J105731.17+405646.1	GPS	G	53	94	266	105	535	783	264	197	0.66	LEG	-4.93	Type2
J112027.80+142055.0	GPS	Q	2	19	86	71	77	93	29	36	0.67	LEG	-3.13	Type2
J113138.89+451451.1	CSS	Q	5	11	64	24	74	76	55	47	0.89	LEG	-2.62	Type1 ^b
J115727.60+431806.3	CSS	Q	30	77	1051	36	320	163	66	57	1.69	HEG	-1.38	Type1
J120624.70+641336.8	CSS	Q	3	51	513	35	290	141	61	70	1.53	HEG	-1.97	Type1
J124419.96+405136.8	CSS	Q	13	87	237	56	152	230	112	90	0.48	LEG	-2.25	Type1 ^a
J125226.35+563419.6	CSS	Q	14	315	2774	114	1408	517	233	183	1.63	HEG	-1.44	Type1
J132513.37+395553.2	GPS	G	34	90	114	119	408	394	291	232	0.25	LEG	-4.00	Type2
J134035.20+444817.3	GPS	G	20	219	660	58	1365	682	246	195	1.20	HEG	-1.96	Type2
J134733.36+121724.2	GPS	Q	18	163	481	654	1201	1193	618	461	0.57	LEG	-2.93	Type1 ^a
J140028.65+621038.5	GPS	Q	3	9	87	33	131	71	18	21	1.44	HEG	-2.43	Type2
J140700.39+282714.6	GPS	Q	47	543	2794	979	2139	2045	579	519	0.93	LEG	-1.97	Type1
J140942.44+360415.9	CSS	Q	10	79	298	76	270	246	108	80	0.83	LEG	-2.22	Type2
J143521.67+505122.9	CSS	G	18	23	53	24	161	221	101	73	0.58	LEG	-3.55	Type2
J151141.26+051809.3	HFP	Q	30	118	898	220	487	410	289	250	1.01	HEG	-2.23	Type1 ^a
J152349.34+321350.2	CSS	G	17	25	292	34	136	309	70	78	1.13	HEG	-2.34	Type2
J154525.48+462244.3	CSS	Q	3	54	321	96	328	175	115	80	1.12	HEG	-3.01	Type2
J155927.67+533054.4	CSS	G	25	36	149	31	136	214	71	64	0.77	LEG	-2.74	Type2
J160246.39+524358.3	CSS	G	26	37	111	48	199	401	185	125	0.51	LEG	-3.61	Type1 ^a
J160335.16+380642.8	CSS	G	8	11	54	32	92	84	81	44	0.80	LEG	-3.79	Type2
J160913.32+264129.0	GPS	Q	3	33	145	130	138	109	28	83	0.72	LEG	-2.57	Type1 ^b
J161148.52+404020.9	CSS	Q	14	94	394	175	567	691	388	374	0.72	LEG	-2.58	Type2
J164348.60+171549.4	CSS	G	25	13	81	39	69	249	23	21	0.76	LEG	-3.36	Type2
J225025.34+141952.0	CSS	Q	36	201	1451	37	718	411	136	109	1.52	HEG	-1.14	Type1

Columns are listed as follows: (1) object name; (2) radio type: CSS/GPS/HFP/CSO; (3) source SDSS classification: G - galaxy, Q - quasar; (4) median signal-to-noise ratio of the spectrum; (5) - (11) The flux of each narrow emission line in units of $10^{-17} \text{erg s}^{-1} \text{cm}^{-2}$ with typical uncertainty of $< 10\%$; (12) the EI index; (13) HEG and LEG classification based on EI index (separation: 0.95); (14) the estimated Eddington ratio ($L_{\text{bol}}/L_{\text{edd}}$); (15) optical classification based on whether the existence of the broad lines. (^a: the source have broad lines and σ_* measurements; ^b: the source have broad lines measurements but $D_{4000} > 1$ and $\text{SN} < 10$)